

Lunar volcanic gas cloud chemistry: Constraints from glass bead surface sublimates



T.A. Williams^{a,*}, S.W. Parman^a, A.E. Saal^a, A.J. Akey^b, J.A. Gardener^b, R.C. Ogliore^c

^a Department of Earth, Environmental, and Planetary Sciences, Brown University, Providence, RI, United States of America

^b Center for Nanoscale Systems, Harvard University, Cambridge, MA, United States of America

^c Department of Physics, Washington University in St. Louis, St. Louis, MO, United States of America

ARTICLE INFO

Dataset link: [Data from Lunar Volcanic Gas Cloud Evolution: Constraints from Glass Bead Surface Sublimates \(Original data\)](#)

Keywords:
The moon(1692)
Volcanism(2174)
Lunar mineralogy(962)

ABSTRACT

Lunar pyroclastic glass beads preserve a record of physical and chemical conditions within volcanic gas clouds in the form of nanoscale minerals vapour-deposited onto their surfaces. However, the scale of these mineral deposits - less than 100 nm - has presented challenges for detailed analysis. Using SEM, TEM, APT, and NanoSIMS, we analysed pristine black glass beads from Apollo drive tube 74001 and found a sequence of sulfide deposition that directly evidences lunar gas cloud evolution. The deposits are predominantly micromound structures of nanopoly-crystalline sphalerite ((Zn,Fe)S), with iron enrichment at the bead-micromound interface. Thermochemical modelling indicates that hydrogen and sulfur were major elements within the volcanic plume and ties the iron gradient to decreasing gas pressure during deposition. This pressure drop may also be consistent with our observed trend of potential $\delta^{34}S$ depletion. Finally, Apollo 17 74220 orange beads, deposited higher in the Shorty Crater sequence, appear to lack abundant ZnS nanocrystals ([Liu and Ma, 2024a](#)), suggesting a change in vapour deposition between orange- and black-glass bead deposition. Together, our results suggest a change in eruption style over the course of a pyroclastic volcanic eruption in the Taurus-Littrow Valley.

1. Introduction

Analysis of lunar volcanic samples has revealed that at least some of the moon's mantle retains volatile contents comparable to Earth's depleted upper mantle ([Hauri et al., 2015; Saal et al., 2008](#)). Evidence for high volatile contents comes from the products of pyroclastic eruptions that occurred between 3.3 and 3.6 Ga ([Snyder et al., 1992](#)). Fragmentation during these volcanic eruptions generated sub-millimetre sized melt droplets, which quenched into glass beads as they travelled through the eruption cloud ([Rutherford et al., 2017; Snyder et al., 1992](#)). The pressures, temperatures, and volatile element compositions of the lunar volcanic gas clouds are recorded by these glass beads, which preserve evidence of three stages of evolution along their path through the plume: 1) outgassing, 2) ingassing, and 3) desublimation/condensation ([Saal et al., 2008; Su et al., 2023; Varnam et al., 2024; Fig. 1](#)).

In stage 1, the partial pressures of volatile elements (e.g., H, S, Cl) in the gas cloud surrounding the molten beads are below their equilibrium vapour pressures. This gradient results in diffusion-controlled outgassing of volatile species, leading to their depletion from the molten beads.

Decreasing volatile element concentrations from the cores to the rims of the beads provides evidence for this outgassing ([Saal et al., 2008](#)). Volatile loss is also recorded in the discrepancy between high volatile concentrations in melt inclusions trapped within olivine phenocrysts, and relatively low concentrations found within their host beads ([Hauri et al., 2011; Ni et al., 2019; Su and Zhang, 2024; Wetzel et al., 2015](#)).

During stage 2, the beads progress into cooler, lower pressure regions of the gas plume, further from the vent. Cooling leads to the equilibrium vapour pressures of many degassed volatile species becoming lower than their partial pressures in the plume, reversing their activity gradients. The resultant diffusive ingassing of the bead is recorded in diffusive profiles of some elements that increase in the outer rim (~50 µm) of the glass beads (e.g., Na, K, Cu, and S; [Su et al. \(2023, 2025\)](#)).

Finally, in stage 3, as the beads enter the more rarefied extremities of the gas cloud, the temperature falls below the glass-melt transition temperature, and the molten beads quench to glass. Contemporaneously, moderately volatile elements (e.g., S, Zn) become oversaturated within the gas cloud, driving the nucleation of mineral phases both homogeneously in the gas cloud, and heterogeneously on the surfaces of the glass beads ([Henley and Berger, 2013](#)). These mineral phases are

* Corresponding author.

E-mail address: thomas.williams@brown.edu (T.A. Williams).

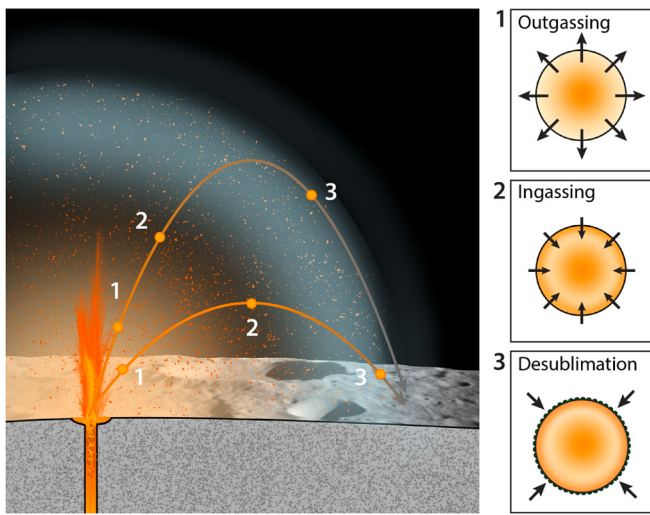


Fig. 1. Schematic diagram of a lunar lava fountaining volcanic eruption. Two glass bead trajectories through the volcanic gas cloud are illustrated with the arrowed lines (one lofted, one shallow). Three stages of bead evolution are depicted: 1) outgassing, 2) ingassing, 3) desublimation/condensation. This follows the unified model for bead evolution proposed by Su et al. (2023). Beads on different trajectories will encounter different conditions during stage 3 along different path lengths. In this paper we identify the minerals condensed onto the surface of the glass beads during stage 3. We then use thermodynamic modelling to constrain the pressure and temperature conditions within the gas cloud when the minerals were formed.

deposited as nanoscale (<100 nm thick) coatings on the surfaces of glass beads (McKay et al., 1973). Although these minerals are de-sublimated and/or condensed phases, in line with historical terminology, we refer to them as sublimate minerals, or, simply, sublimes.

The composition and mineralogy of the sublimes are controlled by the pressure, temperature, oxygen fugacity ($f\text{O}_2$), and chemical composition of the volcanic gas cloud from which they formed (Renggli et al., 2017; Liu et al., 2020; Renggli and Klemme, 2020). Analysis of the sublimes and their deposition sequence should therefore provide improved constraints on these parameters for degassing and diffusion models (e.g., Saal et al. (2008), Su et al. (2023)), particularly with respect to gas pressure, which remains unknown (Renggli et al., 2017; Head et al., 2020; Su et al., 2023).

Sublimate layering will record systematic temperature evolution over the course of mineral precipitation, as minerals with high melting/sublimation temperatures and low volatility will have precipitated at higher temperatures than those with low melting temperature and high volatility (Pokrovski et al., 2013). Additionally, as the exact sequence of deposition depended on the major volatile gas composition, the mineralogy and layering within the sublimes will allow us to determine conditions spatially along glass bead trajectories through the eruptive cloud. Beads with different trajectories can end up in the same place (Fig. 1). Therefore, we expect that beads from a single sample should show a diversity of sublimate stratigraphies.

Historically, efforts to identify and analyse the sublimate minerals were hampered by their nanometric scales and irregular geometries, and therefore their mineralogical composition has traditionally been inferred from molar ratios in leachates (Heiken et al., 1974; Chou et al., 1975; Meyer Jr. et al., 1975; Goldberg et al., 1975; Wasson, 1976; Heiken and McKay, 1977; Clanton et al., 1978). Improvements in spatial resolution and detection limits, as well as sample handling techniques, now allow for the identification and analysis of sublimate minerals, and for the imaging of stratigraphy within the sublimate coating. As a result, Zn, Zn-S, S, and Si layers have been imaged on the surfaces of glass beads from Apollo soil 15401 using TEM (Ross et al., 2011). Additionally, high-resolution SEM has revealed the presence of Na-K-sulfates and zinc

chlorohydroxosulfates on glass beads in Apollo sample 74220 (Ma and Liu, 2019a; Liu and Ma, 2022), ZnS nanocrystals on samples 15366, 73001, and 15426 (Liu et al., 2020; Liu and Ma, 2024a; Ma and Liu, 2023), NaCl nanocrystals on pristine black beads from sample 73001 (Liu and Ma, 2024b), and Fe and FeS condensates on yellow beads from sample 15426 (Ma and Liu, 2024).

The primary goal of this study is to use sublimate coatings on pristine Apollo 17 black glass beads to provide constraints on the pressure, temperature, $f\text{O}_2$, and chemical composition of lunar volcanic plumes. Our approach is twofold. First, we employ a comprehensive suite of nanoanalytical tools (Scanning Electron Microscopy (SEM), Energy-Dispersive X-ray Spectroscopy (EDS), Transmission Electron Microscopy (TEM), Electron Energy Loss Spectroscopy (EELS), Nanoscale Secondary Ion Mass Spectrometry (NanoSIMS), and Atom Probe Tomography (APT)) to determine the mineralogy, elemental composition, and isotopic variations of sublimes hosted on 74001,431 glass beads. Second, we use thermodynamic modelling to evaluate lunar gas speciation models by comparing their speciation predictions with the observed mineralogy, and then constrain the pressure-temperature- $f\text{O}_2$ space over which de-sublimation of the observed minerals occurs.

Although the sublimate minerals are reactive in air (Liu and Ma, 2022; Ma and Liu, 2019a; McKay and Wentworth, 1992; Ross et al., 2011), most previously analysed lunar glass beads have been exposed to the atmosphere. We analyse drive tube samples that have not been exposed to atmospheric air and transfer them between analytical equipment in air-free transfer shuttles, thereby preserving the pristine nature of the sublimes.

2. Methods

2.1. Sample description

The samples are high-Ti glass beads extracted from sample 74001,431. Using transmitted and reflected light microscopy, we characterised all analysed beads as black. These black glass beads were collected in a double drive tube during Apollo 17 from a depth of ~0.5 m on the south rim of Shorty Crater. They were transported from the moon sealed in the drive tubes before being stored under nitrogen at NASA Johnson Space Centre, and thus have not been exposed to Earth's atmosphere. Three sets of analytical work were performed on different sub-samples of the beads, as detailed in Fig. 2.

Our entire SEM, TEM and APT analytical procedures were completed without atmospheric exposure; the samples were shipped and opened under nitrogen and moved between analytical instruments via Leica VCT100 transfer systems and SemiLab STS transfer shuttles. The only samples exposed to air prior to analysis were those allocated for NanoSIMS work. All analytical work and sample handling except for NanoSIMS was conducted at the Centre for Nanoscale Systems, Harvard University.

2.2. SEM-FIB sample preparation

A Zeiss Crossbeam 550 scanning electron microscope (SEM) was used to identify regions of interest for subsequent transmission electron microscopy (TEM) and atom probe tomography (APT) on 36 beads. Imaging was performed in secondary electron mode at an accelerating voltage of 1 kV.

We extracted two ~120 nm thick TEM lamella from two separate black beads (beads I and II). A thin layer of focussed ion beam (FIB) deposited Pt was placed on top of the region of interest for TEM prior to sample lift-out to protect the sample surface from Ga^+ ion beam damage during the cutting and milling processes.

Specimens for APT were created from sublimes on four additional black beads (III, IV, VII, and VIII) following a standard focused ion beam lift-out protocol (Thompson et al., 2007) using a Zeiss Crossbeam 550. Before lift-out, the bead surfaces were capped with Cr via in-situ ion-

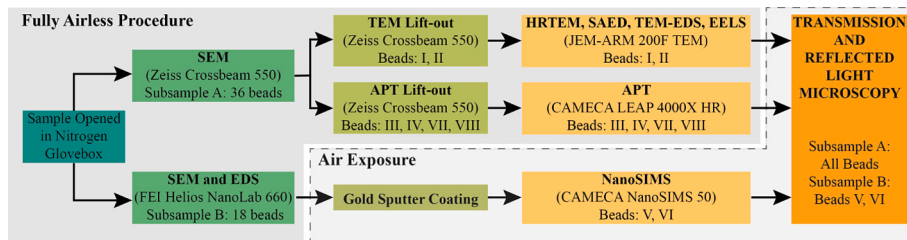


Fig. 2. Flowchart summarising the three analytical procedures applied to individual beads. Beads I and II were analysed using TEM, TEM-EDS, and EELS; beads III and IV were analysed using APT; and beads V and VI were analysed using NanoSIMS. TEM and APT analyses were conducted entirely without air exposure. Beads were selected based on surface morphology; beads I, IV, V, and VI host only micromounds, while beads II, III, VII, and VIII host both micromounds and lathes (section 4.1).

beam redeposition to protect the surface from ion beam damage (Woods et al., 2023), and to increase the diameter of the finished cone where it intersected with the surface of the sublimates. This increased the field of view in the APT to improve counting statistics and enabled steady-state analysis conditions to be approached before evaporation of the sample (Prosa et al., 2019). The apex diameters of the APT needle-shaped samples were prepared to be <100 nm.

Black glass bead samples for NanoSIMS analysis were mounted on carbon tape and imaged using a FEI Helios NanoLab 660 DualBeam Scanning Electron Microscope (SEM). Both secondary electron and backscattered electron signals were acquired, with an accelerating voltage of 2 kV for both imaging modes. Additional compositional information was obtained with an EDAX X-ray Energy Dispersive Spectrometer (EDS). After SEM analyses, the beads were prepared for NanoSIMS work by sputter coating them with a conductive gold layer. The NanoSIMS samples were briefly exposed to air (~ 2 min) during transfer into the sputter coater, then left in air after the gold coating had been applied, distinguishing this analysis sequence from our other airless procedures. Although the gold coating likely does not fully protect the samples from reaction with air (Lee et al., 2004; McKay and Wentworth, 1992), NanoSIMS analyses are minimally affected as a result of this exposure.

2.3. STEM-EDS-EELS analysis

TEM, Electron Energy Loss Spectroscopy (EELS), and Energy Dispersive X-ray Spectroscopy (EDS) data were collected using a JEM-ARM 200F TEM equipped with Gatan Enfinium ER Dual EELS and EDAX Octane W 100 mm^2 EDS spectrometers. The STEM was operated at 200 keV with a ~ 0.1 nm probe diameter. The EELS spectra were acquired as spectrum images. For the high-loss EELS measurements, the energy resolution (measured as the full width at half maximum of the zero-loss peak) was 4.3 eV with an energy dispersion of 1.0 eV/ch, 340 pA probe current, a convergence angle of 30 mrad, and an exposure time of 0.026 s. EELS data were analysed using DigitalMicrographTM (Gatan). EDS spectra were analysed post-collection using TEAM EDS Smart Quant, with standardless quantification achieved via an inbuilt Cliff-Lorimer ratio technique.

2.4. Atom probe tomography (APT) analysis

Three-dimensional APT data was acquired on a CAMECA LEAP 4000X HR. The specimens were field evaporated at a base temperature of 43.6 K under laser-pulsing mode in an ultrahigh vacuum (7.5×10^{-12} Torr). The laser energy was set at 60 pJ with a pulse frequency of 100 kHz and a detection rate of $\sim 0.5\%$. The evaporated ions were projected onto a position-sensitive detector, allowing for the reconstruction of their original positions and identification based on their mass-to-charge ratios (Reddy et al., 2020). 3D reconstruction and data analysis was conducted using the AP Suite 6.1 software package. SEM images acquired before and after the final milling of each tip were used to assist in

the reconstruction. Detailed data acquisition conditions and a data summary of the two APT tips successfully analysed in this study can be found in Table 1.

All peaks with a height greater than twice that of the background level in the spectrum were identified, and the range of mass-to-charge-state ratio (m/z) values that defined the width of each peak determined manually. To validate our APT mass spectra element selection, we used correlative EELS and TEM EDS measurements to justify peak identification. The mass resolving power ($R_m = m/\Delta m$) on peaks of interest ranged from approximately 450 to 1000. In cases where isobaric interferences were present, the elemental contributions to each peak were estimated using a spectral deconvolution algorithm based on the methodology of Gopon et al. (2019).

To achieve deconvolution, we first determined the integrated area under each peak of interest in the APT data set, and then used a grid search to find the proportions of each element that best reproduced the relative counts at each peak. We defined the best-fit combination as the one that minimised the sum of squared residuals between the grid-search output and the measured values. Within this optimisation routine, all combinations of isotopes were considered equally likely, and the relative amounts of each isotope were based on their natural abundances. A complete description of our algorithm can be found in Supplement 1.

The uncertainty from background noise is negligible for all major peaks. However, a complete determination of uncertainty would require

Table 1
Atom probe tomography (APT) data acquisition conditions and data summary.

Specimen/Data Set	Tip 1 (Bead III)	Tip 2 (Bead IV)
Instrument Model	LEAP 4000X HR	LEAP 4000X HR
Instrument settings		
Laser wavelength (nm)	355	355
Laser pulse energy (pJ)	60	60
Pulse frequency (kHz)	100	100
Evaporation control	Detection rate	Detection rate
Target detection rate (ions/pulse)	0.5 %	0.5 %
Nominal flight path (mm)	382.00	382.00
Sample temperature (K)	43.60	43.50
Chamber pressure (Torr)	7.5×10^{-12}	7.5×10^{-12}
Data summary		
Analysis software	AP Suite 6.1	AP Suite 6.1
Total ions:	7,000,454	40,000,241
Single	4,214,189	23,540,748
Multiple	2,775,404	16,424,285
Partial	10,861	35,208
Time-independent background (ppm/ns)	27.4	22.7
Reconstruction		
Final specimen state	intact	intact
Pre-/post-analysis imaging	SEM/n.a.	SEM/n.a.
Radius evolution model	Tip Profile	Tip Profile
Field factor (k)	3.3	3.3
Image compression factor	1.65	1.65
Assumed E-field (V/nm)	33	33
Detector efficiency	0.36	0.36
Vinitial; Vfinal (V)	1209; 5204	2012; 5574

incorporating full instrumental uncertainty estimates, which is beyond the scope of the current work.

2.5. Nanoscale secondary ion mass spectrometry (NanoSIMS) analysis

A CAMECA NanoSIMS 50 at Washington University in St Louis was used to map ^{32}S and ^{34}S isotope abundances in profiles through the condensate layer on beads V and VI to investigate changing isotopic fractionation throughout the deposition of the condensates.

Prior to ion imaging the analysed areas were cleaned and implanted with Cs^+ by pre-sputtering with a high-current primary Cs^+ ion beam for about approximately 5 min ($\sim 507 \text{ pA}$ beam current). We ceased pre-sputtering when the ^{32}S count rate rose, indicating that we had removed the gold coating. Once pre-cleaning was completed, we acquired negative secondary ion images of the isotopes (^{32}S and ^{34}S) by rastering (256×256 pixels, $1000 \mu\text{s}/\text{pixel}$) a focused primary Cs^+ beam (7.8 pA , 100 nm spot size, 16 kV energy) over a $10 \times 10 \mu\text{m}^2$ sized area in multi-collection mode for analysis. Secondary ion images were recorded simultaneously for both isotopes. To reduce the effects of instrumental drift, we applied a peak correction every 2 cycles, and measured the Cu_2S standard before and after measuring each site (sample-standard bracketing). We used a high mass resolving power ($m/\Delta m = 5900$) to resolve the interference between $^{16}\text{O}_2$ and ^{32}S . This sequence was carried out on a total of 2 areas on 2 different beads. After each analysis, we moved the sample stage to a new area and repeated the sequence.

Raw ^{32}S and ^{34}S ratios were used to calculate delta-values relative to the Cu_2S standard via the equation:

$$\delta^{34}\text{S} = \left(\frac{\left(\frac{^{34}\text{S}}{^{32}\text{S}} \right)_{\text{sample}}}{\left(\frac{^{34}\text{S}}{^{32}\text{S}} \right)_{\text{standard}}} - 1 \right) \times 1000\% \quad (1)$$

Uncertainty in the $\delta^{34}\text{S}$ values within our sample areas was calculated via the bootstrap method. We defined regions of interest (ROIs), avoiding raster-edges. We resampled the pixels in each ROI, allowing repeats, for the total number of pixels (256×256 pixels) and recalculated the $^{34}\text{S}/^{32}\text{S}$ ratio. We did the same for the Cu_2S standard, then recalculated the $^{34}\text{S}/^{32}\text{S}$ values for the sublimate ROIs relative to the standard. We calculated 10,000 bootstrap replicates for each area and calculated the standard deviation of the two distributions. Our 2σ error of $\delta^{34}\text{S}$ is assumed to be twice the standard deviation of the bootstrap distribution. This uncertainty estimate accounts for both statistical uncertainty and systematic variation within the ROIs.

Statistical analyses were performed using R version 4.4.2 (R Core Team, 2024). A weighted linear least squares regression was used to evaluate the relationship between variables, and the significance of the regression was assessed using an F-test and R^2 as a measure of goodness of fit. Differences in mean $\delta^{34}\text{S}$ values between the base and the surface of the sublimate micromounds were tested using a weighted Student's *t*-test (Pasek and Tahk, 2021). Statistical significance was determined as a *p* value below 0.05.

2.6. Thermodynamic modelling

We used thermodynamic modelling to investigate the pressure, temperature, and $f\text{O}_2$ conditions within the lunar gas cloud under which sublimate deposition occurred. This was achieved via a Gibbs free energy minimisation approach using HSC Chemistry™.

The HSC Chemistry™ software package uses standard free energy databases to calculate gas-solid equilibrium. Notably, it does not account for solid-solution, so all predicted phases are pure endmembers. The major element compositions of the gas cloud (C, H, S, F, Cl) were the same as in Renggli et al. (2023) and Varnam et al. (2024). Metals (Fe, Zn,

Ga, Cu, Pb, Ni, Na, K) were incorporated in trace amounts (0.001 mol%) to investigate metal speciation without influencing the speciation of the bulk gas cloud, in a process reflecting that used by Renggli et al. (2023). The metals are included as elemental metallic gases, as well as gas and solid compounds with S, Cl, O, and F. We calculated the mole fraction of all phases of interest over a temperature from 500°C to 1350°C , pressure from 10^{-6} bar to 10 bar, and $f\text{O}_2$ from IW-2 to IW, covering a broad set of $f\text{O}_2$ conditions relevant to the moon (Wadhwa, 2008; Renggli et al., 2017). For each fixed pressure, we determine the quantity of $\text{O}_2(\text{g})$ required to match the offset from the IW buffer at 1350°C , calculating $f\text{O}_2$ using the Excel spreadsheet *Calculate fO2 Buffer* (1.5) (Iacovino, 2022). We select this eruption temperature because the 0 kbar liquidus for the 74220 orange glass beads has been experimentally constrained to approximately $1323\text{--}1369^\circ\text{C}$ (Delano and Heiken, 1990; Green et al., 1975), and the presence of olivine in Apollo 17 orange glass bead samples (Hauri et al., 2011) suggests that 74220 erupted at or slightly below its liquidus temperature. All input parameters and possible gas and solid species are available in the data repository associated with this paper.

To investigate the effect of H on sublimate speciation, we systematically increase the molar abundance of H from 10^{-5} mol% to 80 mol%, keeping molar C, H, S, F, and Cl contents the same as Varnam et al. (2024), and fixing oxygen content at 1350°C .

3. Results

3.1. Scanning electron microscopy (SEM) analysis

SEM analysis of the black glass bead surfaces in both subsamples revealed that the majority of observed surface features, and therefore the majority of potential sublimate phases, are accounted for by four distinct morphology classes: micromounds, lathes, blebs, and plaques (Figs. 3, 4).

The micromounds (Fig. 3b, c) have a predominantly hemispherical geometry with thicknesses approximately equal to their radii, although some appear to have been mechanically deformed, and flattened onto the bead surface (potentially during sample mounting). Most micromounds are 20–30 nm in diameter, but although the micromounds on any individual bead are approximately uniform in size, there is considerable size variability between micromounds on different beads (4–60 nm). There are also large differences in electron beam sensitivity between micromounds on different beads. Under a 1 kV electron beam, some micromounds rapidly develop holes, while others show greater resistance to beam-induced damage. They are classic examples of the micromounds documented on both orange and green glass beads (McKay et al., 1973; Heiken et al., 1974; Clanton et al., 1978; Ma and Liu, 2019b).

Blebs are geometrically similar to micromounds but larger (100–300 nm in diameter) and with greater asymmetry (Fig. 3c). Lathes are defined by an acicular geometry, with a long axis 50–600 nm long, a uniform width of ~ 50 nm, and a height ranging from 50 to 100 nm (Fig. 3c). Plaques are less than 10 nm thick, and group in linear trails across the surface of the bead, seemingly tracing partially buried needle-like crystals embedded within the glass (Figs. 4, S2.1).

There is a significant range in the abundance and extent of sublimate coatings on different beads. The coatings range from sparsely distributed individual micromounds with patches of bare glass (Fig. 3a) to beads that host a mass of sublimate sufficient for micromounds to overgrow one another and create deposits with a botryoidal texture. The curvature of the beads did not allow for the full surface of every bead to be imaged, and therefore the true distributions of sublimate types on the analysed beads may not have been captured. Nevertheless, the analysis revealed a pattern of co-occurrence among the morphology classes with three primary groups of beads emerging: (1) just micromounds, (2) micromounds and blebs, or (3) micromounds, blebs, and lathes (Table 2). The presence of micromounds on any given bead was a prerequisite for the

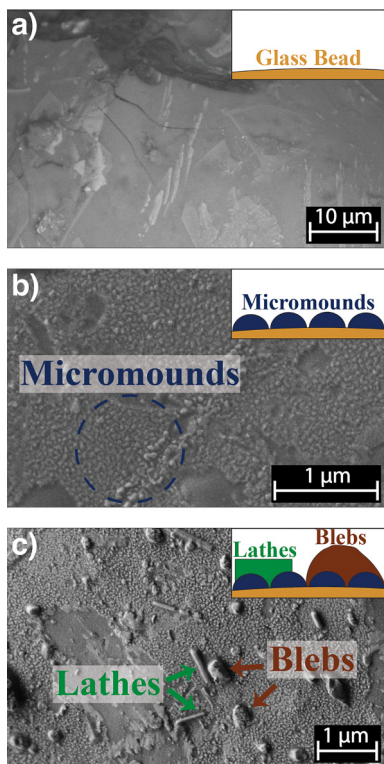


Fig. 3. Secondary electron images of sublimates acquired at an accelerating voltage of 1 kV. Annotations highlight three proposed morphological classes: micromounds, lathes, and blebs. In the top-right corner, schematic illustrations depict the sequential de-sublimation process on glass bead surfaces: (a) Melt droplets quench onto glass beads (here a black glass bead with internal crystallinity); (b) Sublimate mounds form on the glass surface; (c) Lathes and blebs are deposited over the mounds.

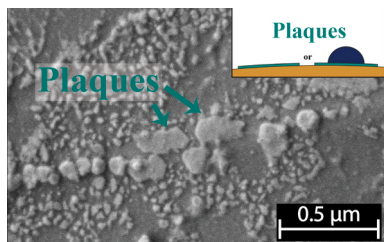


Fig. 4. Secondary electron images of the surface of a lunar glass bead, highlighting two different surface features: mounds and plaques. The plaques follow a linear trend across the surface, appearing above an embedded crystal phase. The schematic illustration in the top-right corner indicates that we have not constrained the position of the plaques within the depositional sequence.

Table 2

Co-occurrence of observed sublimate types on the 36 analysed lunar glass beads in subsample A. The table shows the distribution of sublimate morphologies across analysed beads, with tick marks (✓) indicating the presence and dashes (–) indicating the absence of a given morphology. Three primary groups of beads emerge: (1) beads with only micromounds, (2) beads hosting micromounds, blebs, and lathes, and (3) beads hosting micromounds and blebs. Single occurrences may represent rare morphological distributions or potential misidentifications. We do not include data from subsample B in this table, as we do not consider the imaging coverage to be comprehensive enough to group the beads.

Group	Micromounds	Blebs	Lathes	Plaques	Observations
1	✓	–	–	–	13
2	✓	✓	✓	–	12
3	✓	✓	–	–	8
4	✓	✓	✓	✓	1
5	–	–	–	–	1
6	✓	✓	–	✓	1

appearance of other morphology types, and they are by far the most abundant phase hosted on the surfaces of the beads. The simultaneous presence of all four morphological types on a single bead was only observed once. Additionally, each bead displayed a unique distribution and proportion of the four surface morphologies.

Secondary electron imaging reveals lathes and blebs draping over micromounds, both in plan view (e.g. Fig. 3c), and in FIB cut cross-sections (e.g. Fig. 7). We do not observe micromounds on the surfaces of either lathes or blebs. This suggests deposition of sublimate micromounds preceded the deposition of lathes and blebs. The occurrence of several blebs overgrowing lathes is interpreted to have resulted from either sequential deposition or simultaneous growth. We have insufficient observations to constrain the position of plaques within the depositional sequence.

Fractured bead surfaces were typically devoid of sublimes, with clean glass exposed. Surfaces showing signs of abrasion only occasionally bore sublimate micromounds, typically situated above the scrape marks (Fig. 5b). Vesicles that intersect with the bead surface bear sublimes in the same manner as the rest of the bead (Fig. 5d). Small glass spheres are found embedded within the surface of larger beads (Fig. 5a), likely the result of low-velocity collisions during the eruption (Heiken et al., 1974). Sublimes are hosted on the surface of these embedded glass spheres. In some locations, glass coats the bead surface, and sublimate deposits terminate at the bead-glass interface (Fig. 5c). Similar observations were recorded by Heiken et al. (1974), and must result from impacts that occurred after micromound deposition, but before complete solidification of the colliding droplets.

A preliminary assessment of sublimate composition was conducted using Energy Dispersive X-Ray Spectroscopy (EDS). However, even at low accelerating voltages (<5 kV), this method primarily probed the glass bead material beneath the sublimes due to large excitation volumes, making comprehensive compositional analysis challenging (see Ma and Liu (2019a), Liu et al. (2020)). Therefore, we did not determine the composition of the micromounds, lathes, plaques, or blebs through SEM EDS. However, a thick deposit of NiS with an amoeboid texture was identified on a single bead (Fig. S2.2, S2.3), and the micromounds on both beads selected for NanoSIMS analysis contained Zn and S (Fig. S2.4).

3.2. Transmission electron microscopy (TEM) results

3.2.1. TEM energy dispersive X-ray spectroscopy (EDS) results

TEM-EDS was used to identify elemental distributions and abundances within the micromounds and lathes.

Micromounds: Zn and S are co-localised within the sublimate micromounds (Fig. 6) in approximately equi-atomic proportions (Fig. 12), and their signal intensities are highly correlated, with a Pearson correlation coefficient >0.93 in every analysed micromound (Supplement 3). A limited amount of Fe and O was detected. Oxygen is predominantly located in trace quantities towards the micromound surfaces. However, the generation of X-rays via electron backscattering

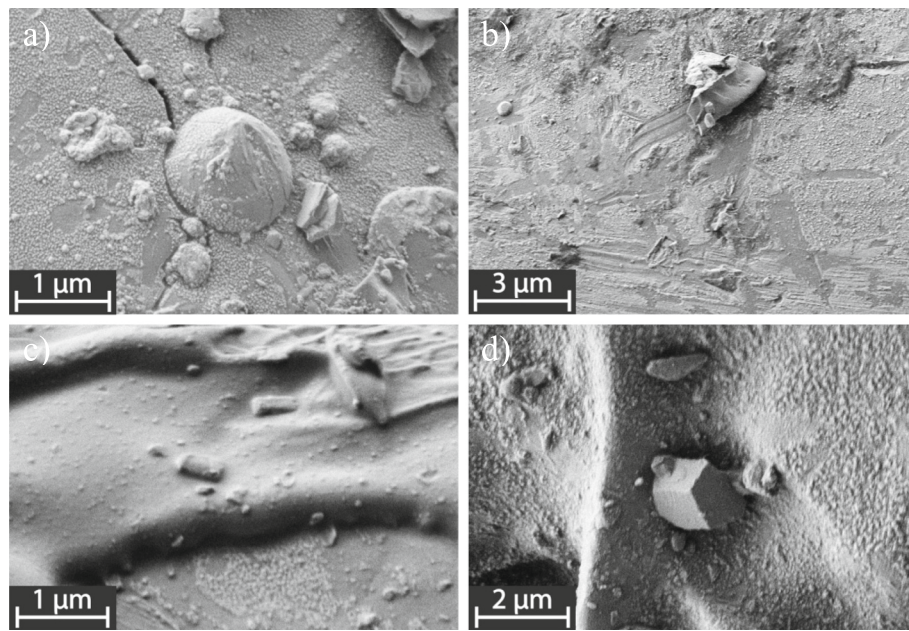


Fig. 5. SEM images of features on the surface of 74001 black glass beads: a) glass sphere embedded within a larger glass bead, with a fracture in the surface to the left of the implanted sphere. Micromounds are hosted on the surface of the sphere; b) the micromounds have been removed through abrasion. Some micromounds remain, possibly due to incomplete removal, or continued deposition following abrasion; c) Glass coating the surface of the beads, including the micromounds; d) micromounds on the surface of a vesicle within the glass bead. Small angular lithic fragments from the regolith have adhered electrostatically to the surface.

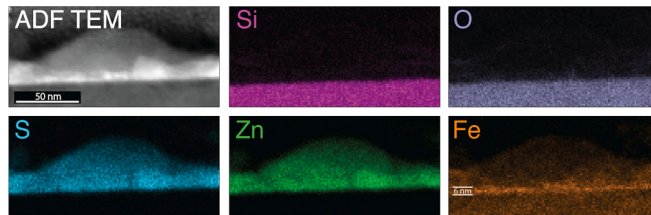


Fig. 6. TEM images of a micromound on bead II. a) Close-up annular dark field (ADF) scanning TEM image showing the sublimate mound structure. Elemental EDS maps for (b) Si, (c) O, (d) S, (e) Zn, and (f) Fe reveal the distribution of these elements within the sublimate mound. S and Zn are the main constituents within the mound and are co-localised. Fe exhibits a notable enrichment along the interface between the bead surface and the base of the mounds, suggesting a distinct boundary layer. The silicate glass bead is identified by a high areal density of Si and O.

in the underlying (oxygen-rich) glass may introduce a spurious oxygen signal within the sublimates (Merli et al., 2003). Fe appears to be enriched in a zone approximately 6 nm thick at the base of the micromound along the glass-sublimate interface on bead II (Fig. 6), but not bead I (Fig. 8). Quantification of both Fe and O within the micromounds was impractical due to low signal strength.

Although detected on other glass bead samples (e.g., Liu and Ma, 2022, 2024a), K and Cl were not detected above background levels in the sublimate micromounds. A trace Na signal was observed, but a portion of this may be attributed to interference between Zn L- and Na K-shell emission lines. Signals attributed to other elements were predominantly categorised as detector noise and secondary fluorescence, in addition to fluorescence of the Cu support grid by bremsstrahlung radiation. Ga and C signals were the result of contamination from our FIB sample preparation procedure.

Lathes: Compositional analysis shows that the lathes have a heterogeneous makeup (Fig. 7). Zn is present throughout the lathes, but the lather cores contain Zn in excess of S (Fig. 12), along with minor amounts of Fe. In contrast, Fe and S are absent in the outer rims, which instead exhibit higher concentrations of Si and O. We were unable to identify

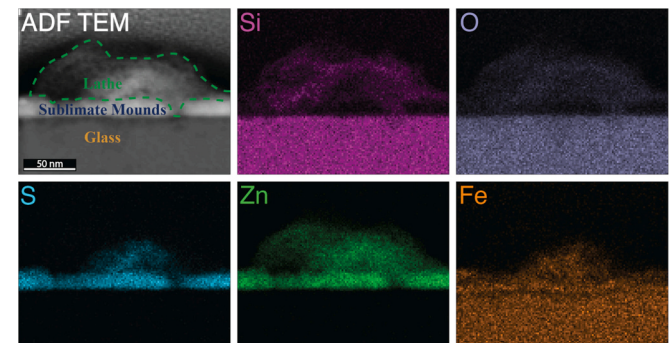


Fig. 7. TEM images of sublimate coating on bead II. a) Close-up annular dark field (ADF) scanning TEM image showing a sublimate lathe overlying multiple mound structures. Elemental EDS maps for (b) Si, (c) O, (d) S, (e) Zn, and (f) Fe reveal the distribution of these elements within the sublimate mound. S and Zn are the main constituents within the mound and are co-localised. The silicate glass bead is identified by a high areal density of Si and O.

any known stoichiometric mineral corresponding to either the core or the rim. These data suggest that the core of each lather may be partially composed of Zn^0 , while the outer rim may consist of a mixed Zn-silicate mineral phase.

Additional features: Ni-rich regions, with diameters approximately between 5 and 10 nm, were identified at the surface of the bead, above ilmenite crystals embedded within the glass (e.g., Fig. 8). These Ni-rich phases do not exhibit significant co-localisation with the primary elements within the micromounds (S and Zn). However, they do appear to co-occur with O and Fe. Due to their small size, significantly less than the ~120 nm thickness of the TEM lamella, accurate quantification is challenging due to signal contributions from underlying materials, as well as detector noise. These are unconnected to the amoeboid Ni-containing mass observed with SEM.

3.2.2. Electron energy loss spectroscopy (EELS) results

Unlike EDS, the EELS signal from within the micromounds does not

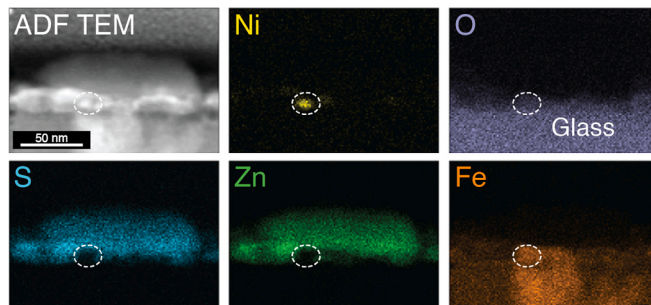


Fig. 8. TEM images of sublimate coating on bead I. a) Close-up annular dark field (ADF) scanning TEM image showing the sublimate mound structure. Elemental EDS maps for (b) Ni, (c) O, (d) S, and (e) Zn, and (f) Fe reveal the distribution of these elements within the sublimate mound. S and Zn are the primary constituents of the mound and are co-localised. Small Ni-rich, S-poor phases are embedded in the glass surface, with the location of the Ni particle outlined by a dashed white line. The vertical Fe-rich feature embedded within the glass is identified as an ilmenite crystal.

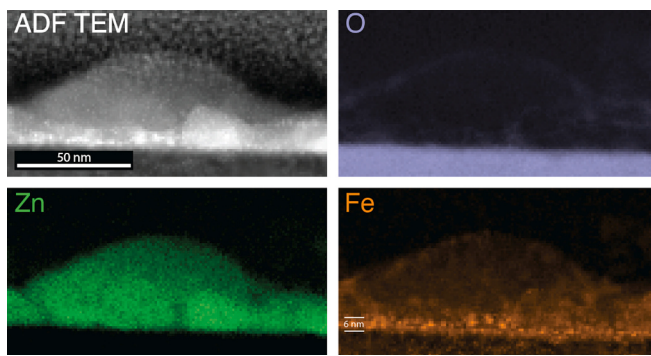


Fig. 9. TEM images of the same sublimate micromound on bead II as in Fig. 6. (a) Close-up annular dark field (ADF) scanning TEM image showing the sublimate mound structure. Elemental EELS areal density maps for (b) O, (c) Zn, and (d) Fe reveal the distribution of these elements within the sublimate mound. O exhibits only a trace presence within the mound. Zn is a primary constituent, consistent with EDS measurements. Fe is concentrated in a distinct layer at the base of the mound.

receive a contribution from the underlying glass through electron backscattering (Collins and Midgley, 2017). Additionally, electron energy loss peaks overlaps occur for different elements than characteristic X-ray emission peaks, enabling more definitive peak identification through correlative use of the two techniques.

A pronounced Zn L-edge signal was identified throughout the micromounds (Fig. 9). Mirroring our EDS results, a thin (~6 nm) layer exhibiting a significant increase in Fe concentration was observed at the base of the sublimate micromound. Slightly enhanced Fe L-edge areal densities were also detected at the outer edges of the micromounds. Given limitations in spatial resolution, compounded by potential signal contributions from both glass and sublimate due to TEM lamella tilt, the precise nature of this Fe-enriched layer - whether a distinct iron phase, or greater iron sulfide solid-solution within a zinc sulfide – could not be conclusively determined.

The oxygen signal derived from the sublimates was weak compared to that from the glass, with only a slight enrichment observed near the surfaces of the micromounds (Fig. 9). A low signal-to-noise ratio for the S L-edge precludes accurate determination of sulfur distributions using EELS.

3.2.3. Selected area electron diffraction (SAED) results

The micromounds are subdivided into nano-crystalline clusters ~10 nm thick and appear to be amorphous in many areas (Fig. 10a). Within

the crystalline regions, prominent d-spacings at 0.307 nm and 0.191 nm were identified using TEM SAED (Fig. 10 a, b). These spacings are consistent with the (111) and (220) lattice planes of sphalerite respectively (Downs and Hall-Wallace, 2003). Our measured mean (111) spacing of 0.308 nm is offset from that of pure sphalerite (~0.312 nm) by ~1.3 %. This discrepancy is consistent with the effects of solid solution of impurities such as Fe and Cu on the lattice structure (Buzatu et al., 2013; Deng et al., 2019).

3.3. APT results

Atom Probe Tomography (APT) was employed to better quantify elemental abundances within the micromounds and identify any 3D nano-scale elemental distributions or layering. We prepared two tips through the sublimate micromounds (beads III and IV), and APT measurements were carried out successfully on both tips. We also prepared two tips through the sublimate lathes (beads VII and VIII), but neither yielded successful data acquisition, as the lathes delaminated during field evaporation due to poor adhesion to the bead surface.

The distributions of selected ions within the atom probe needle extracted from bead III are displayed in Fig. 11. APT analysis confirms the presence of Zn as a primary constituent within the sublimate micromounds and detected minor amounts of Fe (5.9–7.3 ionic %) and Cu (max. 3.6–4.0 ionic %). Na is present at less than 0.3 ionic %, but neither K nor Cl are detectable above the background.

Limited mass-charge resolution precluded definitive identification and quantification of oxygen and sulfur peaks due to isobaric interferences. For instance, Zn^{2+} , O_2^+ , and S^+ ions all exhibit a prominent peak at a mass-to-charge ratio (m/z) of 32 Da, which is present ubiquitously throughout the sample (Fig. S1.3, S1.4). However, our EELS data revealed that micromound oxygen concentrations are negligible. Additionally, the 16 Da $^{16}O^{+}/^{32}S^{2+}$ peak was far more abundant in the glass than the micromound. We therefore excluded oxygen as a candidate element within the sublimate micromounds during peak identification. Based on this criterion, spectral decomposition analysis determined that Zn and S are present in approximately equal proportions within the micromounds, with a slight S excess relative to Zn (Fig. 12). Although this approach does not give highly accurate values for the proportion of each species at each peak, it does provide reasonable constraints at the level of accuracy we require.

Fe is enriched in an ~6 nm thick zone along the boundary between the Zn-rich sublimate and the underlying glass (Fig. 13). It is possible that the difference in field evaporation potential between surface atoms in the sublimate micromound and the glass results in a different electrostatic field required for field evaporation across the sublimate-glass boundary (Dhara et al., 2018). This could lead to preferential loss of species from either phase, biasing the compositional measurement (Hatzoglou et al., 2020; Rousseau et al., 2023). However, our correlative workflow using EDS and EELS demonstrates that iron enrichment towards the base of the sublimate micromound is not the result of analytical artefacts. Due to isobaric interferences between glass-hosted oxygen and sublimate-hosted sulfur (e.g., $^{16}O^{+}$ and $^{32}S^{2+}$ at 32 Da, $^{16}O^{+}$ and $^{32}S^{2+}$ at 16 Da) we cannot determine whether the iron is present as Fe, FeS, or FeO using APT alone. No Ni-rich regions were encountered during APT analysis.

3.4. NanoSIMS results

We obtained one NanoSIMS profile through the sublimates on bead VI (Fig. 14). The $\delta^{34}S$ values are all negative relative to our standard. The weighted linear least squares fit of the data was $\delta^{34}S = -41.72 + 0.93x$, and the overall regression was statistically significant ($R^2 = 0.517$, $F(1,19) = 20.37$, $p < 0.001$). The $\delta^{34}S$ value at the surface of the sublimate micromounds is significantly more negative (Mean = -40.64‰, SD = 7.11‰) than at the base of the sublimate micromounds (Mean =

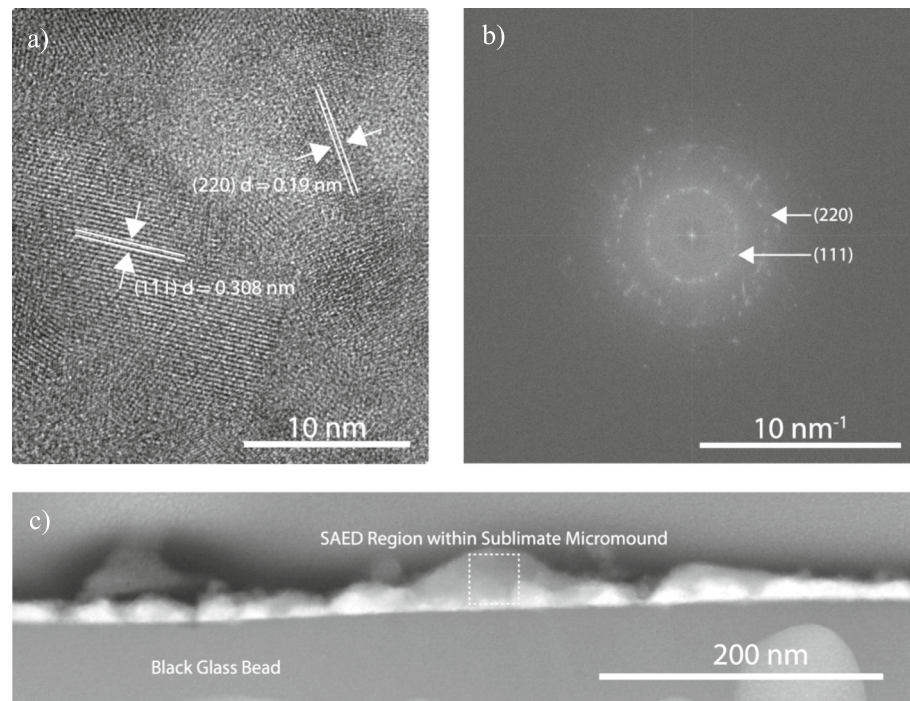


Fig. 10. (a) High-resolution TEM (HRTEM) image of a sublimate mound with annotated lattice planes, corresponding to the (111) and (220) planes of sphalerite. (b) Fast Fourier Transform (FFT) pattern from the same sublimate mound, confirming the crystallographic orientation. (c) TEM dark field image of sublimate mounds on the surface of glass bead II, with the region of interest for (a) and (b) indicated. This region is the same as that shown in Figs. 6 and 9.

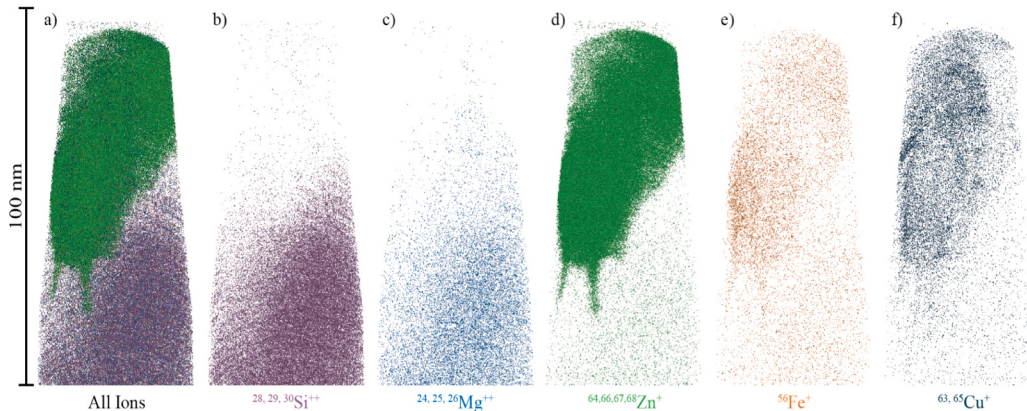


Fig. 11. APT ion point clouds of the whole specimen (bead IV). a) all ions within the tip. Additional maps show the presence of: b) Si, c) Mg, d) Zn, e) Fe, and f) Cu. Zn and Fe are co-localised within the sublimate mound at the top left of the tip. The underlying glass is visible due to a significant enrichment in Si and Mg ions.

-11.20% , SD = 12.20%), $t(3.22) = 3.56$, $p = 0.034$. $\delta^{34}\text{S}$ values do not correlate with ^{32}S or ^{34}S yields, suggesting that isotope ratio variations are not due to yield changes.

3.5. Thermodynamic modelling results

We observe solid Fe, Ni, and Zn species on the surfaces of the 74001 black glass beads. We therefore investigate the speciation of solid Fe, Ni, and Zn species within the volcanic gas cloud using the major element abundances of Renggli et al. (2023) and Varnam et al. (2024). We also investigate Na and K speciation, as Na and K phases have been observed on other lunar glass bead samples (e.g., Liu and Ma (2022, 2024a)).

We assume that sublimate deposits were only preserved below the $\sim 938 \text{ K}$ quench temperature of the beads (Arndt and Engelhardt, 1987). Below this temperature, $\text{ZnS}_{(\text{s})}$ is the primary solid host phase for Zn, and $\text{FeS}_{(\text{s})}$ is the primary solid host phase for Fe (Fig. 15 a,e). Although native

metal and oxides solid species become more abundant with decreasing pressure (Fig. 15 b,c,f,g), and solid metal chlorides become more abundant with increasing pressure (Fig. 15 d,h), no pressure control is significant enough to result in detectable amounts of Zn or Fe precipitating as native metal, oxide, or chloride solids under equilibrium conditions. Oxygen fugacity exerts only a minor control on Fe and Zn speciation (Fig. S2.6). Ni speciation patterns are similar to that of Zn (Fig. S2.7), likely because both are transition metals with a 2^+ valence state under lunar-relevant $f\text{O}_2$ conditions (Steenstra et al., 2020).

We investigate gas cloud P-T controls on the formation of the Fe-enriched nanolayer by considering the micromounds to be a mechanical mixture of the sphalerite endmembers $\text{ZnS}_{(\text{s})}$ and $\text{FeS}_{(\text{s})}$. At any given pressure, $\text{FeS}_{(\text{s})}$ stabilises at higher temperatures than $\text{ZnS}_{(\text{s})}$, and the lower the vapour pressure in the gas cloud, the greater the temperature difference between the condensation of solid $\text{FeS}_{(\text{s})}$ and $\text{ZnS}_{(\text{s})}$ species (Fig. 15). Therefore, as the volcanic gas cloud expands into the lunar

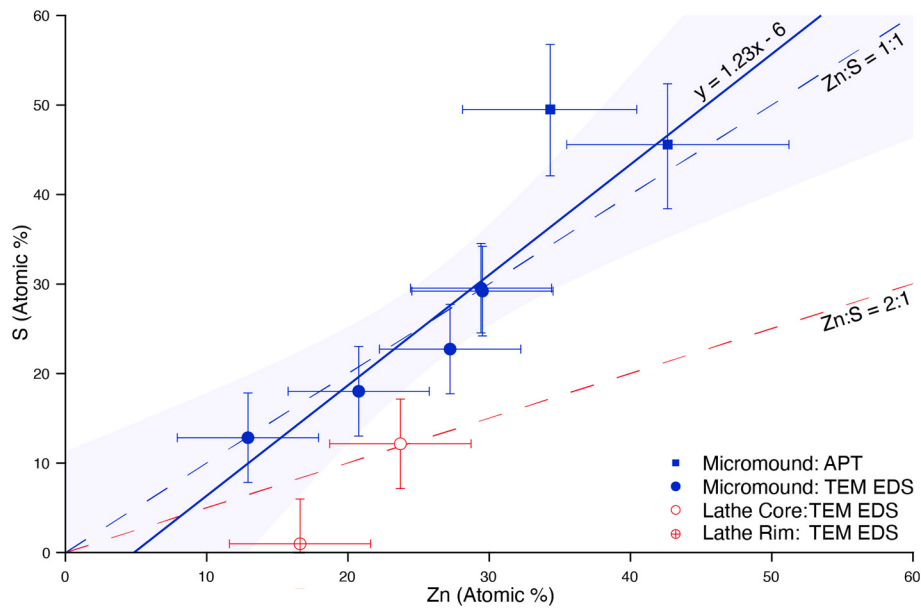


Fig. 12. Zn/S ratios in sublimate micromounds and lathes analysed via TEM EDS and APT. The blue circles and squares represent EDS and APT quantification of micromounds respectively. The red circles represents EDS quantification of a lathe. The standard error of the TEM EDS quantification is estimated to be $\pm 5\%$. The 95 % confidence intervals for APT quantification are derived from a Monte Carlo error propagation method that accounts for uncertainties in the best-fit spectral deconvolution parameters, and do not include errors from data ranging. A weighted linear regression of the mound Zn and S abundances is plotted as a solid blue line ($y = 1.2337x - 5.9881$, $R^2 = 0.837$), with the shaded blue region representing the 95 % confidence intervals of the regression. Variations in quantified Zn and S abundances from TEM are attributed to differences in sample thickness relative to the TEM lamella, affecting the intensity of the X-ray signal from the micromounds. (For interpretation of the references to colour in this figure legend, the reader is referred to the web version of this article.)

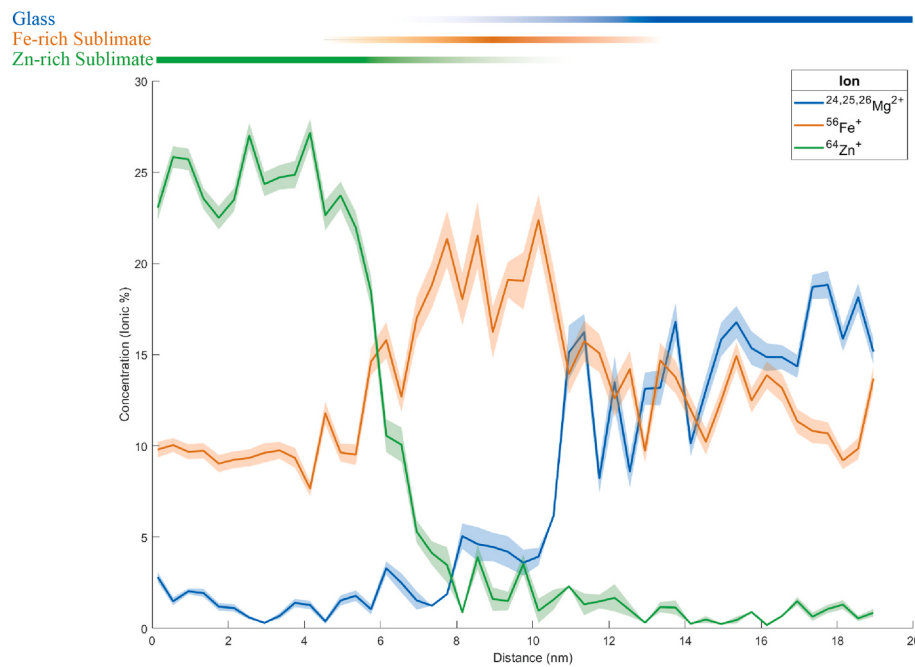


Fig. 13. One dimensional concentration profile of ions normal to the sublimate-glass boundary on bead III detected using APT. This profile demonstrates the enrichment of iron across the boundary. The sublimate is represented by $^{64}\text{Zn}^+$, the interface by $^{56}\text{Fe}^+$, and glass by $^{24,25,26}\text{Mg}^{++}$. These regions are delineated by the bars at the top of the plot, showing that the interface is not sharp within the APT dataset. The species were chosen to minimise isobaric interferences. $^{24,25,26}\text{Mg}^{++}$ has no major peak overlap within the sample, $^{56}\text{Fe}^+$ has a minor interference with $^{28}\text{Si}^+$, and $^{64}\text{Zn}^+$ has an interference with $^{32}\text{S}^+$. The shaded regions represent the standard deviation of the data, which does not account for error introduced from ranging the data.

environment, with a consequent decrease in temperature and pressure, it is possible that the ratio $\text{ZnS}_{(s)}/\text{FeS}_{(s)}$ in the condensing phase increases (Fig. 16a). Although this simple approach does not account for second-order effects such as solid solution, a transition from initial high-FeS precipitation to low-FeS precipitation as a result of decreasing

temperature would be consistent with the expected cooling pathway of the lunar gas beads through a lunar volcanic gas cloud.

We also investigate the predicted abundance of $\text{NaCl}_{(s)}$ due to its observation on Apollo 17 black glass beads in Liu and Ma (2024a). We predict that $\text{NaCl}_{(s)}$ should have a similar abundance to $\text{ZnS}_{(s)}$ when bulk

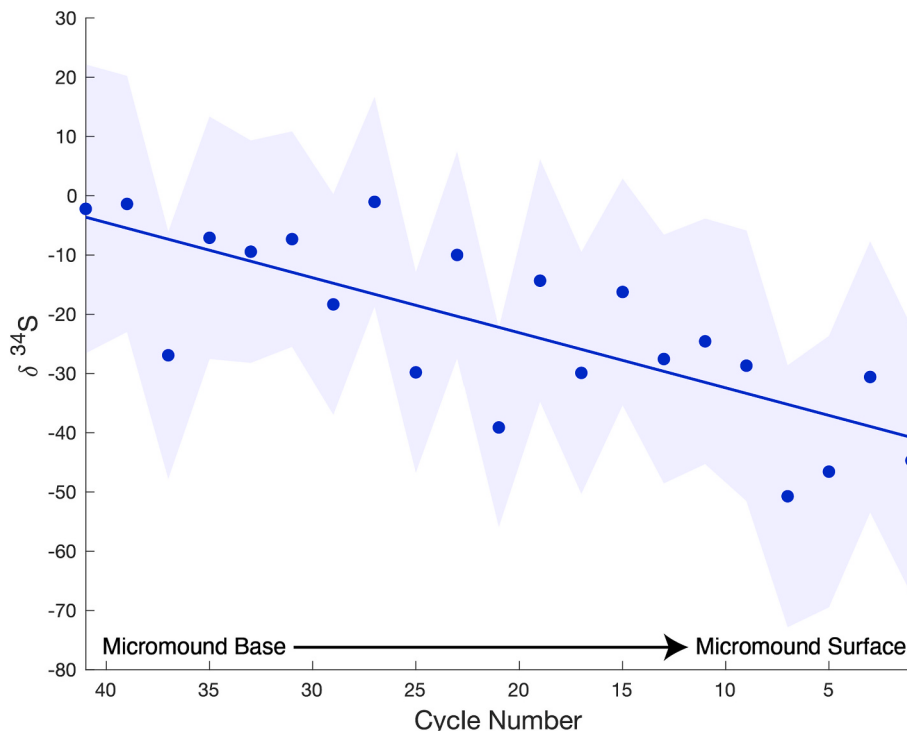


Fig. 14. Sulfur isotope ratios ($\delta^{34}\text{S}$) of the sample (bead VI) plotted against the number of NanoSIMS analytical cycles. Each circle represents an individual sulfur isotope measurement. The shaded region indicates the 1σ uncertainty on each point derived from bootstrap resampling ($n = 10,000$). The solid black line denotes a weighted linear regression through the data ($R^2 = 0.517$). The sulfur isotope composition of the Cu_2S reference material is defined as 0‰. These data are reproducible within combined internal (cycle-to-cycle) and external (standard-based) uncertainties, as indicated by the 1σ error bars.

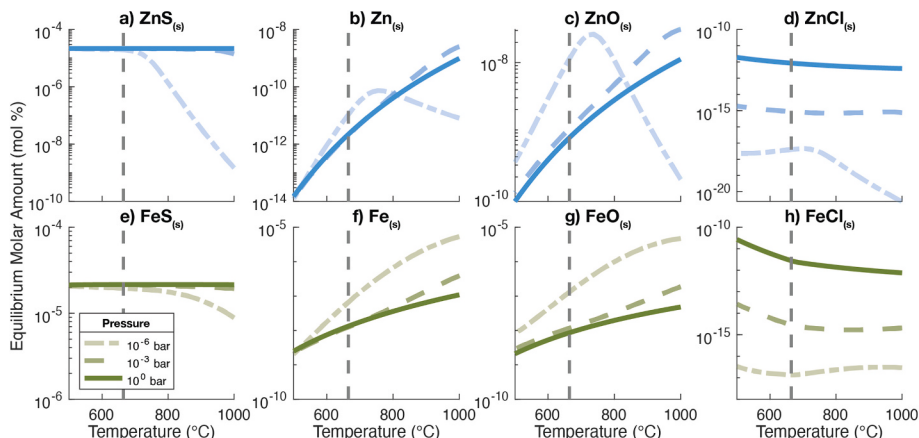


Fig. 15. Equilibrium molar abundances of solid Zn and Fe compounds at IW-1 at 10^0 , 10^{-3} , and 10^{-6} bar using the major volatile element composition derived by Varnam et al. (2024). The plots illustrate how the equilibrium concentrations of these compounds vary with both temperature and pressure. The vertical dashed line represents the 938 K glass transition temperature for High-Ti Orange Glass Beads (Arndt et al., 1984). Results for the major volatile element composition of Renggli et al. (2023) are shown in Fig. S2.5.

Zn and Na in the gas cloud are identical, except within a narrow low P-T band (Fig. 16b). $\text{NaF}_{(s)}$ is predicted to be present in slight excess of $\text{NaCl}_{(s)}$ using the inputs of Renggli et al. (2017), whereas $\text{NaCl}_{(s)}$ is present in excess of $\text{NaF}_{(s)}$ if the inputs of Varnam et al. (2024) are used (Fig. S2.9, S2.10). The molar abundances within Varnam et al. (2024) are likely more relevant to high-Ti glass beads.

Finally, we investigate the effect of H abundance within the gas cloud. Below the bulk abundance ratio $H/(F + Cl) \lesssim 1$, $\text{ZnCl}_2{}_{(s)}$ is the primary solid zinc phase across the entire P-T- $f\text{O}_2$ space, and the molar abundance of $\text{ZnS}_{(s)}$ is orders of magnitude lower (e.g., Fig. 17). To be consistent with $\text{ZnS}_{(s)}$ condensation on bead surfaces rather than $\text{ZnCl}_2{}_{(s)}$, the condition $H/(F + Cl) \gtrsim 1$ must thereby be satisfied.

4. Discussion

4.1. Composition and mineralogy of the sublimate layer

The sublimate micromounds on the surfaces of the four lunar black glass beads from which we obtained compositional information are comprised of nano-polycrystalline sphalerite - $(\text{Zn}_{x},\text{Fe}_{1-x})\text{S}$ - and exhibit solid solution with a range of elements (primarily copper). Iron is enriched at the base of the sublimate micromounds and is likely bonded to sulfur. This iron enrichment is either the result of higher molar amounts of FeS dissolved within $(\text{Zn}, \text{Fe})\text{S}$ at the base of the micromound compared to the top, or the presence of a separate FeS species mixed

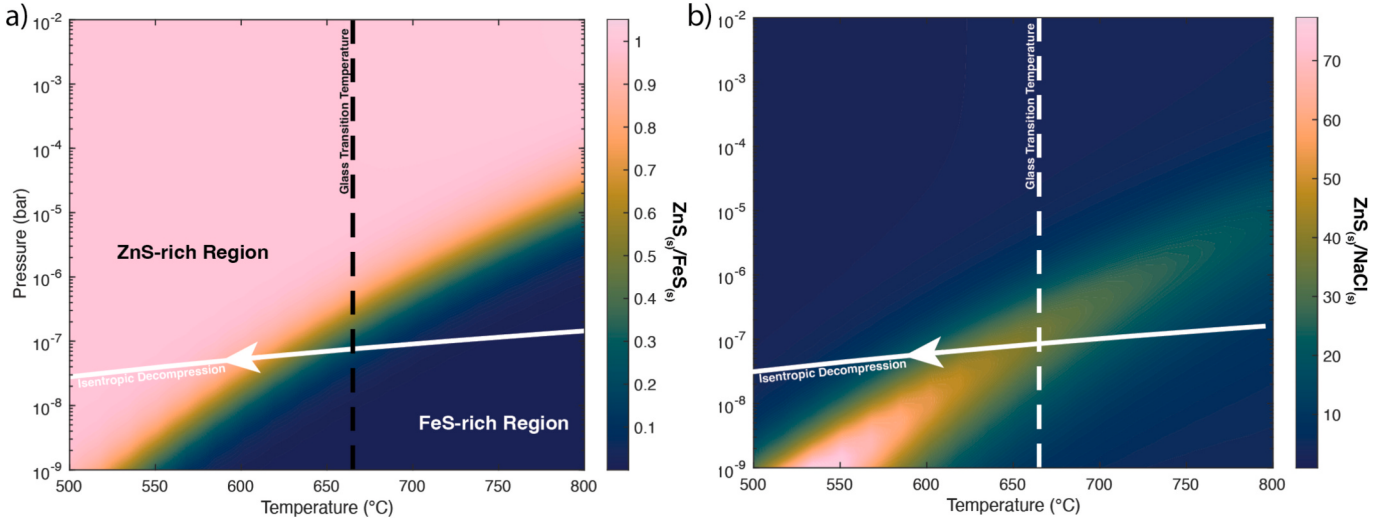


Fig. 16. Illustration of the molar ratio of a) $\text{ZnS}_{(s)}$ to $\text{FeS}_{(s)}$ and b) $\text{ZnS}_{(s)}$ to $\text{NaCl}_{(s)}$ in the lunar volcanic gas cloud over a range of temperatures and pressures at IW-1 at $1350\text{ }^{\circ}\text{C}$, using the volatile element composition of Renggli et al. (2023). The diagram highlights the stabilisation of $\text{FeS}_{(s)}$ over $\text{ZnS}_{(s)}$ at elevated temperatures and reduced pressures. The white line represents an isentropic expansion pathway of the gas cloud, following the simplified approach of Renggli et al. (2017). The initial conditions start from an arbitrary pressure within the region where $\text{FeS}_{(s)}$ is more abundant than $\text{ZnS}_{(s)}$. These results suggest that it is possible to initially precipitate $\text{FeS}_{(s)}$, followed by $\text{ZnS}_{(s)}$ as the cloud cools and expands. This mechanism may account for the observed higher iron concentration at the mound's base. $\text{ZnS}_{(s)}$ and $\text{NaCl}_{(s)}$ are predicted to have a similar abundance except within a narrow band at low pressure. $\text{KCl}_{(s)}$ abundance mirrors that of $\text{NaCl}_{(s)}$ (Fig. S2.8).

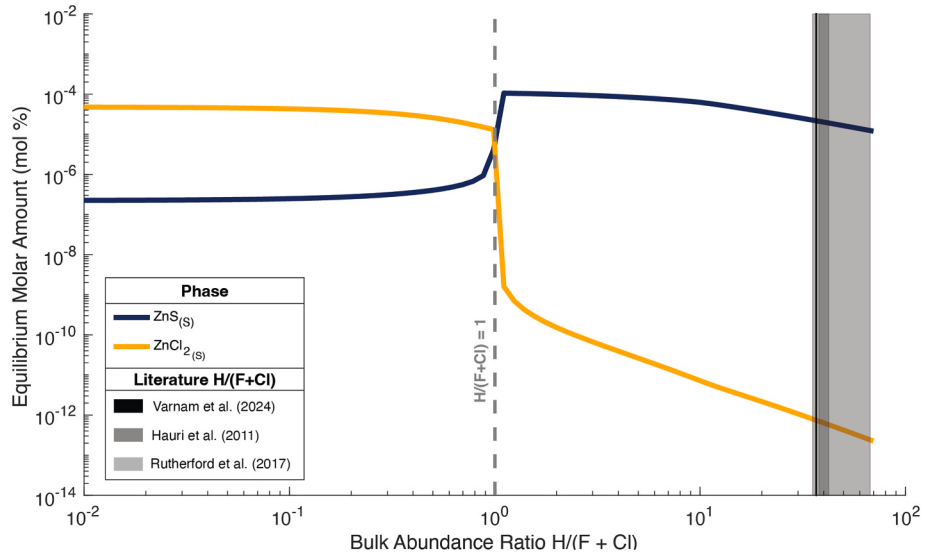


Fig. 17. Equilibrium molar amounts of $\text{ZnS}_{(s)}$ and $\text{ZnCl}_2{}_{(s)}$ as a function of the bulk molar abundance ratio $\text{H}/(\text{F} + \text{Cl})$ in a lunar volcanic gas cloud at $700\text{ }^{\circ}\text{C}$, 1 bar. This plot illustrates how the availability of hydrogen relative to fluorine and chlorine influences the formation of solid zinc sulfide and zinc chloride. At $\text{H}/(\text{F} + \text{Cl})$ ratios less than 1, hydrogen is primarily consumed by HCl and HF , leading to a higher prevalence of $\text{ZnCl}_2{}_{(s)}$. Conversely, at ratios greater than 1, excess hydrogen is available after Cl and F are bound, favouring the formation of $\text{ZnS}_{(s)}$. Grey shaded regions represent the range of $\text{H}/(\text{F} + \text{Cl})$ ratios reported by Rutherford et al. (2017), Varnam et al. (2024), and Hauri et al. (2011). Details of these calculations are found in Supplement 5. The $\text{H}/(\text{F} + \text{Cl}) = 312$ ratio in Renggli et al. (2023) falls to the right of this figure, indicating conditions strongly favouring the formation of $\text{ZnS}_{(s)}$. Models 3–6 in Fegley (1991) fall to the left of the unity ratio ($0.017\text{--}1.67 \times 10^{-6}$), indicating that they contain an unrealistically low H abundance. The ratio will change with time from initially high to lower values as magma decompression progresses, and Cl and F exsolution increases their abundance in the gas.

with sphalerite. The thickness of the Fe-rich layer is too thin to enable explicit observation of iron sulfide species such as troilite or pyrrhotite within the micromounds. However, because Fe abundances within the micromounds are below the 20–30 mol% FeS required for $(\text{Fe}, \text{Zn})\text{S}$ phase separation under equilibrium conditions (Barton and Toulmin, 1966; Lusk and Calder, 2004), we argue that Fe enters solid solution within the sphalerite lattice rather than forming a separate phase.

On Earth, co-precipitation of multiple metal-sulfide minerals assemblages is often observed in volcanic mineral deposits (Henley and Berger, 2013). Although all sublimate micromounds in this study were

composed of sphalerite, only a limited number of micromounds were analysed, making it possible that additional minerals also exhibit this morphology on bead surfaces (Sabri et al., 2014). The range of sensitivity to electron beam damage displayed by micromounds on different beads suggests that the micromounds are composed of materials with differing susceptibilities to electron beam evaporation, likely due to mineralogical differences (Egerton et al., 2004). This effect was observed by Liu and Ma (2024a, 2024b), who found that NaCl nanocrystals on 73001 glass beads are beam sensitive, whilst ZnS nanocrystals are not. Together, this indicates that additional non-sphalerite

mineral phases may comprise a portion of the micromounds on some 74001 lunar glass beads, necessitating further investigation to definitively exclude their presence, particularly iron sulfide minerals (e.g., troilite, pyrrhotite), and NaCl (Liu and Ma, 2024a).

The mineralogy of the other sublimate phases - lathes, blebs, and plaques - hosted on the glass beads has not yet been fully characterised. The lathes bear a striking resemblance to the Na-phase reported by Liu and Ma (2022). However, although the chemical heterogeneity of the lathes prevented definitive elemental quantification using TEM EDS, the lathes analysed in this study are a Zn-phase, possibly consisting of native zinc or a zinc silicate mineral.

A more comprehensive future study should aim to characterise the composition of the plaques and blebs. Based on SEM observations alone, it is possible that the blebs represent large micromounds that have undergone extensive growth. However, it is perhaps more likely that they are simply glassy droplets that have adhered to the surface of the beads, rather than products of vapour-deposition.

Although smaller than previously reported metal blebs, the Ni-rich particles detected in this study could be analogues of the Fe-Ni blebs widely observed in Apollo 17 deposits (Weitz et al., 1997, 1999). Consequently, they may form through similar processes involving redox reactions, either during magma ascent within the volcanic conduit, or during cooling, crystallisation, and volatile loss within the volcanic lava fountain (Weitz et al., 1997, 1999).

4.2. Volcanic gas cloud conditions

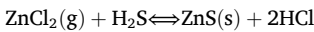
4.2.1. Major volatile elemental (H, C, O, S, Cl) composition

We use our observation that sphalerite is the host phase of Zn in the sublimate layer to assess the validity of the gas cloud compositions and metal-speciation predictions in the thermochemical model of Renggli et al. (2023) and Varnam et al. (2024).

In a gas cloud containing major volatile elements in the same molar proportions as these two models, $\text{ZnS}_{(\text{s})}$ is predicted to be the most abundant solid Zn phase at all temperatures below the glass transition temperature of the glass beads and across the entire modelled pressure range. As our results demonstrate that sphalerite (ZnS) is the Zn host phase in the sublimate layer, we suggest that the gas cloud compositions in Renggli et al. (2023) and Varnam et al. (2024) are accurate to a first-order approximation.

However, these gas cloud compositions are derived from a combination of diffusion modelling and/or analysis of melt inclusions (Hauri et al., 2011; Saal et al., 2008; Varnam et al., 2024), and it has been suggested that bulk elemental abundances within the gas cloud may not be reflective of those derived from these analyses (Varnam et al., 2024). This is because of processes including redox reactions (McCanta et al., 2019; Moussallam et al., 2016), evolving degassed elemental compositions throughout degassing (Ustunisik et al., 2011, 2015), and non-simultaneous degassing (Edmonds and Wallace, 2017; Wilson and Head, 2018). We therefore determine whether bulk volatile contents within the gas cloud can be more tightly constrained by the mineralogy of the micromounds.

We did not observe evidence for ZnCl_2 precipitation; therefore, the H contents of the volcanic plume were greater than the combined F and Cl contents, leading to ZnS precipitation via reactions such as:



(Colson, 1992; Wasson, 1976). This enables us to exclude models 3–6 of Fegley (1991), as they do not contain sufficient H for this reaction to occur. However, gas cloud compositions in Rutherford et al. (2017), Kring et al. (2021), Renggli et al. (2023), and Varnam et al. (2024) do contain sufficient H for this reaction to occur. In all these models, an unrealistically low bulk S content would be required for $\text{ZnCl}_{2(\text{s})}$ to be present in proportions comparable to $\text{ZnS}_{(\text{s})}$. As such, S and Cl proportions relative to one another within the gas cloud at the time of micromound deposition are virtually unconstrained by our

thermodynamic modelling approach, as these species exert a minor influence on volcanic gas chemistry relative to H (Fegley, 1991). Accordingly, we are unable to determine which of the four models most accurately represents the lunar volcanic gas cloud.

We do, however, note that Kring et al. (2021) apply degassing extents from Saal et al. (2008) to the proposed mantle concentrations in Hauri et al. (2011), rather than the pre-degassing contents measured in melt inclusions. This approach yields low volatile element abundances and does not account for partitioning during low-degree mantle melting (Varnam et al., 2024).

In contrast, H/(F + Cl) values reported by Renggli et al. (2023) are significantly higher than other estimates. Renggli et al. (2023) model gas release from green glass beads using diffusion modelling (Saal et al., 2008) rather than using melt inclusions. Additionally, green glasses exhibit noticeably different post-eruption fluorine contents compared to orange glasses (Varnam et al., 2024). These two factors may also contribute to why Liu and Ma (2024a) detected $\text{NaCl}_{(\text{s})}$ on 73001 black glass beads rather than $\text{NaF}_{(\text{s})}$, despite thermochemical models based on the molar abundances of Renggli et al. (2023) suggesting that $\text{NaCl}_{(\text{s})}$ is less abundant than $\text{NaF}_{(\text{s})}$.

Although the high degree of Cl isotope fractionation observed in lunar magmas can only be explained by evaporation of metal chlorides from a magma with substantially less H than Cl (Sharp et al., 2010), the high H/(F + Cl) ratios implied by this study are not incompatible with later H depleted degassing; loss of rapidly diffusing H could occur before Cl degassing is complete (Sharp et al., 2013). This scenario would result in sequential degassing of a vapour with a completely different composition, and future systematic sampling of sublimate mineralogy throughout core depths could be used to investigate this process.

4.2.2. Elemental metal (Zn, Fe, Ni) concentrations

Lunar gas cloud bulk metal contents are poorly constrained (Varnam et al., 2024). In contrast to the major volatile elements, melt inclusions are inadequate for determining vapour-phase metal proportions, as subsurface metal deposition may fractionate metals relative to one another (Henley and Berger, 2013). When Fe and Zn are present in trace bulk quantities within the gas cloud, thermodynamic predictions indicate that the ratio $\text{FeS}_{(\text{s})}/\text{ZnS}_{(\text{s})}$ is approximately the same as the bulk Fe/Zn ratio under most conditions. Because our results demonstrate that $\text{FeS}_{(\text{s})}$ (either dissolved in sphalerite or as a separate mineral) is present in lower quantities than $\text{ZnS}_{(\text{s})}$ on bead surfaces, we suggest that Zn is more abundant in the gas cloud than Fe. We also suggest that a quantitative understanding of sphalerite-vapour Zn and Fe partitioning would allow sphalerite composition to be used to determine Zn/Fe ratios in the volcanic gas cloud.

The observation of a Ni-bearing sublimate on only a single bead, coupled with thermodynamic predictions indicating that Ni is similarly stable to Zn and Fe under lunar gas cloud conditions, suggests that Ni is likely present in lower abundances than both Zn and Fe within the gas cloud.

4.2.3. P-T-fO₂ Constraints

The cooling rates of the glass beads imply quenching in a hot gaseous medium (Hui et al., 2018). We propose that micromounds are the first sublimate phase to precipitate upon glass solidification, followed by the subsequent deposition of lathes (and potentially bleb)-like structures. If the volcanic plume expanded with distance from the vent, this would suggest that the micromounds form in a hotter, denser portion of the gas cloud than the lathes and blebs.

If the blebs represent glass droplets adhered to bead surfaces, rather than vapour-deposited mineral phases, then the sublimate structures hosted on the beads can be classified into two distinct groups: micromounds alone, or micromounds overlain by lathes. This grouping could reflect two distinct populations of glass beads, each of which followed different ballistic trajectories through the volcanic gas cloud before being deposited in the same location (illustrated in Fig. 1). Beads with

only micromounds traversed a shallow trajectory through the hotter, denser portions of the gas cloud where only micromound vapour deposition occurred. Conversely, beads with both micromounds and lathes followed a lofted trajectory, allowing initial micromound deposition in the interior of the plume to be followed by lathe deposition in the colder, more rarefied outer portions of the plume. A larger-scale analysis of a more extensive bead sample set would be required to evaluate the robustness of this distribution. This model also requires refinement to explain the observed variability in the abundance and extent of sublimate coatings on different beads: rather than reflecting just two distinct trajectories, the beads may represent a continuum of trajectories, all of which experienced micromound deposition, but not all of which experienced lathe deposition.

Because $\text{ZnS}_{(s)}$ and $\text{FeS}_{(s)}$ are the most stable Zn and Fe host-phases at all temperatures below the glass-transition temperature, and at all modelled pressure and $f\text{O}_2$ conditions, the bulk mineralogy of the sphalerite micromounds offers limited constraints on the P-T- $f\text{O}_2$ conditions experienced by the beads within the volcanic plume. However, trends in elemental abundances within individual micromounds offer the potential for investigating changing P-T- $f\text{O}_2$ conditions over the course of mineral precipitation. We find that the Fe/Zn ratio in the micromounds is greatest at the start of sublimate deposition (the base of the micromound) and decreases throughout deposition. This decreasing $\text{FeS}_{(s)}/\text{ZnS}_{(s)}$ ratio is replicated in our thermochemical model when gas temperature (and, to a lesser extent, pressure) decreases during deposition. A positive correlation between temperature and the amount of iron that can be accommodated within sphalerite is also observed in physical experiments (Deer et al., 2013; Lusk and Calder, 2004). This temperature dependence between temperature and FeS abundance implies that gas cloud cooling and expansion drives the transition from early high-FeS to late low-FeS sublimate deposition. The transition only occurs at low gas cloud pressure. Therefore, we suggest that the sublimates that did not host an Fe enrichment may have formed at slightly higher gas cloud pressures.

The sensitivity of the $\text{FeS}_{(s)}-\text{ZnS}_{(s)}$ transition to P-T conditions presents an opportunity for future studies to better constrain P-T conditions within the volcanic plume, and to better determine bulk gas Fe/Zn ratios under which such a transition will be present. Such work could follow an experimental approach or utilise a more complete thermodynamic model, and enable the determination of why not all beads host an iron rich layer.

Determining the mineralogy of the lathes, blebs, and plaques may also refine constraints within P-T- $f\text{O}_2$ space, providing a focus for future work. Additionally, analysis of a greater number of glass bead sublimates could enable the absence of predicted stable species at specific P-T-X- $f\text{O}_2$ conditions to eliminate these fields as potential regions within the gas cloud.

4.2.4. Limitations of thermodynamic models to determine volcanic gas cloud conditions

While the Gibbs free energy minimization approach employed by HSC Chemistry™ provides valuable insights into the gas cloud conditions associated with sublimate deposition, its accuracy is constrained by the exclusion of factors such as solid solution, kinetics, and nanoscale thermodynamics, which influence both phase stability and mineral precipitation processes.

We modelled the abundance of pure $(\text{Zn},\text{Fe})\text{S}$ endmember species without incorporating solid solution effects, and with equimolar bulk abundances of Fe and Zn. This will have led to a miscalculation of Gibbs free energy, and the overall equilibrium state predicted by the model will have been less accurate, as solid solutions can stabilise phases and alter the condition under which they form.

Our results only apply if equilibrium was achieved. Equilibrium condensation would have required rapid reaction kinetics relative to the timescale under which P-T- $f\text{O}_2$ conditions change, as well as relatively slow, reversible sublimate deposition. However, it is possible that in the

case of lunar volcanic eruptions, slow reaction kinetics prevented the gas composition from evolving post-fragmentation (Varnam et al., 2024). Additionally, rapid sublimate deposition may have resulted in the precipitation of thermodynamically metastable phases. Gas-solid reaction kinetics are complex, and reliable kinetic parameters are not yet available (Ali et al., 2022). These issues suggest that classical thermodynamics may not be applicable to the dynamic conditions within a lunar gas cloud (King et al., 2018).

Factors such as interfacial tension were not included in the energy minimisation calculations, despite their potential relevance at the nanoscales associated with mineral de-sublimation (Elliott, 2021; Subramani et al., 2023). Below ~ 10 nm in size, surface enthalpies are the leading terms in calculating the nanoscale phase stability (Subramani et al., 2023), and therefore an offset between our bulk thermodynamic stability predictions and nanoscale phase stability is be expected.

Finally, it has been demonstrated that these three limitations have a measurable effect that leads to a misfit between the deposition temperatures predicted by thermodynamic calculations, and the deposition temperatures observed in vapour-deposition experiments (Renggli and Klemme, 2020) and at fumaroles (Wahreberger et al., 2002).

4.3. Sulfur isotope fractionation

Our analyses indicate the sequential deposition of sulfide phases along the beads' trajectory, and our NanoSIMS data indicates a statistically significant $\delta^{34}\text{S}$ depletion of $29.44 \pm 8.28\text{\textperthousand}$ over the course of sublimate deposition. This depletion is consistent with observations of isotopically light sulfur in the coatings of orange and black glass beads (Ding et al., 1983; Dottin et al., 2023; Saal and Hauri, 2021; Thode and Rees, 1976). Furthermore, there is evidence that sulfur isotope fractionation may occur within lunar volcanic gas clouds (Su et al., 2025). To evaluate potential mechanisms driving the isotopic trend, we model sulfur isotope fractionation during the condensation of $\text{ZnS}_{(s)}$ and $\text{FeS}_{(s)}$ from a lunar volcanic gas cloud, considering three fractionation scenarios: closed-system equilibrium, open-system Rayleigh, and kinetic. Results from these models are shown in Fig. S2.11.

To calculate the equilibrium fractionation factor $\alpha_{\text{Solid-Gas}}$ to model closed- and open-system condensation we first calculate the fractionation factor $\alpha_{\text{H}_2\text{S-Gas}_i}$ for sulfur-bearing gases (SO_3 , SO_2 , COS , CS_2 , CS , S_2 and H_2S) in a temperature range from 500 °C to 1000 °C. This calculation utilises equilibrium fractionation factors (β) for exchange reactions between sulfur-bearing species (Richet et al., 1977). We then obtain $\alpha_{\text{Solid-Gas}_i}$ for each sulfur-bearing gas i by subtracting $\alpha_{\text{H}_2\text{S-Gas}_i}$ from the $\alpha_{\text{ZnS-H}_2\text{S}}$ and $\alpha_{\text{FeS-H}_2\text{S}}$ values in Li and Liu (2006). We calculate the bulk sulfur isotope fractionation factors for the ZnS-Gas and FeS-Gas systems by applying a weighted sum. The solid-gas equilibrium fractionation factor ($\alpha_{\text{Solid-Gas}_i}$) for each sulfur-bearing gas species is multiplied by its normalised molar proportion n_i in the thermochemical gas model (section 3.6). The total fractionation factor is then obtained by summing over all the major sulfur-bearing gas species in the system:

$$\alpha_{\text{Solid-Gas}} = \sum \alpha_{\text{Solid-Gas}_i} \cdot n_i \quad (2)$$

Equilibrium fractionation reaches a maximum $\Delta^{34}\text{S}_{\text{equilibrium}}^{\text{ZnS-gas}}$ of 0.62 ‰ at 700 °C, 10^{-6} bar, IW-1, and a maximum $\Delta^{34}\text{S}_{\text{equilibrium}}^{\text{FeS-gas}}$ of 0.80 ‰ at 500 °C, 10^{-6} bar, at the IW buffer (Supplement 4). In general, the magnitude of equilibrium isotope fractionation is expected to increase as temperature decreases (Bigeleisen and Mayer, 1947; Blanchard et al., 2017). However, this trend does not hold for the bulk gas mixture because at lower temperatures, H_2S is predicted to become the dominant sulfur-bearing gas species (Fegley, 1991; Renggli et al., 2023). When we extrapolate the $\text{ZnS-H}_2\text{S}$ fractionation factor ($\alpha_{\text{ZnS-H}_2\text{S}}$) to lower temperatures (Li and Liu, 2006), we find that it remains close to unity, resulting in a $\Delta^{34}\text{S}_{\text{equilibrium}}^{\text{ZnS-H}_2\text{S}}$ value of just 0.4 ‰ at 200 °C. Therefore, the ~ 29 ‰ fractionation change observed in the sublimates cannot be

explained by equilibrium isotope fractionation.

If there is a reservoir effect, and the gas remains in isotopic equilibrium with the solid condensate until the gas phase is fully condensed, S isotope fractionation between the vapour and condensed phases can be determined using the Rayleigh distillation model. For an open system, this can be expressed as

$$\delta_{final} = \delta_{initial} + (1000 + \delta_{initial}) (F_v^{(\alpha-1)} - 1) \quad (3)$$

where $\delta_{initial}$ and δ_{final} are defined as the isotopic compositions of the initial and final states of the condensate (‰), and F_v is the fraction of the sulfur species remaining in the vapour. For closed-system condensation, fractionation is expressed as

$$\delta_{final} = \delta_{initial} + 1000 \left(\frac{1}{\alpha} \cdot \frac{1}{eF_v + 1} - 1 \right), \quad e = \frac{1}{\alpha} - 1. \quad (4)$$

Following these equations, even with 99 % vapour deposition, equilibrium condensation of ZnS and FeS can generate a maximum difference of approximately 4.7 ‰ between $\delta_{final}^{34}S$ and $\delta_{initial}^{34}S$. Such an extensive degree of deposition is unlikely to be achieved, given that the mass of gas in the system significantly exceeds the mass of the sublimate formed (Su et al., 2023). Therefore, equilibrium condensation from a finite reservoir cannot account for the observed fractionation change over the course of deposition.

Equilibrium condensation requires the vapour to have been in thermodynamic equilibrium with the condensate. However, if the partial pressure of species i in the vapour (P_i) was not equal to its equilibrium vapour pressure ($P_{i,eq}$), then the instantaneous fractionation factor incorporated kinetic effects:

$$\Delta^{34}S^{Solid-Gas} = \frac{P_{i,eq}}{P_i} \Delta^{34}S_{equilibrium}^{solid-gas} + \left(1 - \frac{P_{i,eq}}{P_i} \right) \Delta^{34}S_{kinetic}^{solid-gas} \quad (5)$$

As $\frac{P_{i,eq}}{P_i} \rightarrow 0$, the flux becomes unidirectional (from vapour to condensate) and isotopic fractionation becomes mostly kinetic. Assuming that condensation coefficients are identical for different isotopologues (Dauphas and Schäuble, 2015), kinetic fractionation then becomes an entirely mass dependent process prescribed by

$$\Delta^{34}S_{kinetic} = 1000 \left(\sqrt{m_H/m_L} - 1 \right) \quad (6)$$

where m_H and m_L represent the masses of particles with heavy and light isotopes respectively. With this mass dependence, the lighter molecules diffuse to the condensate faster than the heavier molecules, resulting in magnitudes of kinetic fractionation larger than those of equilibrium fractionation ($\Delta^{34}S_{kinetic}^{ZnS-Gas} = -10.1$ ‰, $\Delta^{34}S_{kinetic}^{FeS-Gas} = -10.9$ ‰). Saal and Hauri (2021) use these fractionation values to suggest that significant kinetic isotope fractionation occurs during condensation.

Following eq. 5, we can reproduce the direction of our isotopic trend if sphalerite deposition begins as an equilibrium process, and over the course of deposition the ratio $\frac{P_{i,eq}}{P_i}$ decreases, thereby increasing the contribution from kinetic fractionation. This scenario is plausible, because as distance from the volcanic vent increases, and the gas cloud cools and expands, P_i and $P_{i,eq}$ decrease at different rates. $P_{i,eq} \propto 1/T$ (Berkowitz and Marquart, 1963), whereas $P_i \propto \left(\frac{T_2}{T_1} \right)^{\frac{\gamma-1}{\gamma}}$ under the assumption of isentropic expansion (where T_1 and T_2 are the initial and final temperatures, and γ is the ratio of the heat capacities at constant pressure and constant volume). As such, P_i can exceed $P_{i,eq}$, creating sustained oversaturation during cooling. Furthermore, kinetic fractionation becomes more pronounced as temperatures decrease (Hashimoto, 1990).

Although a transition from equilibrium to kinetic fractionation during condensation produces the greatest $\delta^{34}S$ shift among the mechanisms explored in this paper, none of these processes can fully account for the

total observed sulfur isotope variability. Interestingly, the magnitude of kinetic fractionation expected during condensation of native sulfur ($\Delta^{34}S_{Kinetic}^{S-Gas} = -29.9$ ‰ (Saal and Hauri, 2021)) is sufficient to account for this variability. However, no native sulfur was identified within our samples.

4.3.1. Limitations of NanoSIMS measurements

It is possible that our measured $\delta^{34}S$ change is greater than the true isotopic enrichment through the thickness of the micromounds. If steady-state conditions were not established at the start of our analytical procedure, then progressive Cs^+ implantation within the active domain could have generated an apparent $\delta^{34}S$ trend (Kilburn and Clode, 2013). However, no $\delta^{34}S$ trend was observed for the standard under identical analysis conditions, and the $\delta^{34}S$ trend does not correlate with changes in ^{32}S or ^{34}S yields.

Due to topographic and matrix matching issues, we did not utilise our absolute $\delta^{34}S$ values and focussed solely on the total change during analysis. The samples were mounted whole and could not be polished, resulting in surface topography that may have generated analytical artefacts via the deviation of secondary ion trajectories through electrostatic field deformation (Kita et al., 2009). Charging issues arising from Cs^+ implantation prevented us from using a sphalerite standard, leading to an inadequate Cu_2S matrix match.

Future work should aim to better characterise sublimate $\delta^{34}S$ values and determine whether this trend holds across a larger population of glass beads surface sublimates. Such studies could help validate any potential change in S isotope fractionation within the micromounds and provide new constraints on the evolution of pressure, temperature, and chemical composition within lunar volcanic gas clouds during sublimate deposition.

4.4. Comparison to vapour condensates on other lunar glass bead samples

4.4.1. Volcanic evolution within Shorty Crater deposits

Glass beads from samples 74220 and 74001,431 (this study) are the products of a single eruption preserved on the rim of Shorty Crater (Blanchard and Budahn, 1977; Heiken and McKay, 1977). The 74220 orange glass beads were collected from a 5–8 cm deep surface trench (Meyer, 2010), whereas the 74001,431 glass beads were collected from approximately 50 cm beneath the lunar surface in a core adjacent to the surface trench (Nagle, 1978). As the Apollo 17 glass bead deposits were likely produced during one continuous eruption, these two samples likely represent two time intervals from a single eruption (Blanchard and Budahn, 1977; Heiken and McKay, 1977). As such, investigating differences in surface condensates on these two samples allows us to probe whether mantle source heterogeneity, or gas cloud evolution over the course of volcanic eruptions, controls the mineralogy of condensate phases.

Zinc on 74220 orange glass beads was deposited mainly as Zn metal (Zn^0) which has been altered to Zn-chlorohydroxosulfate (Ma and Liu, 2019a). In contrast, zinc on 74001,431 glass beads was deposited as sphalerite (ZnS) micromounds (this study). Orange glass beads are significantly less abundant in sample 74001,431 than in sample 74220, and orange glass beads exhibit a lower degree of crystallisation (Nagle, 1978). These features suggest that 74220 glass beads cooled more rapidly than 74001,431 glass beads (Weitz et al., 1999). This was likely a consequence of lower gas cloud optical density during 74220 glass bead deposition (Head and Wilson, 2017; Weitz et al., 1999). A lower optical density resulted from lower pyroclastic particle density (Head and Wilson, 2017), which was associated with lower gas pressures.

We therefore determine whether gas cloud pressure controls the difference in Zn deposition between the two bead populations, and find that a transition between ZnS deposition (74001) and Zn^0 deposition (74220) is possible in a gas cloud when pressures fall below $\sim 10^{-6}$ bar. However, with major elements present in the same molar abundances as

reported by Renggli et al. (2023) and Varnam et al. (2024), this transition only occurs at temperatures greater than ~ 900 °C, which exceeds the glass transition temperature of the beads. To explore whether an alternative gas composition could permit detectable Zn^0 condensation below the glass transition temperature, we performed a grid search. Starting with the bulk composition of Varnam et al. (2024), we systematically varied the molar proportion of each species from 0 to 90 mol %, while setting oxygen contents relative to the IW buffer at 1350 °C. No composition was identified in which Zn^0 reached 10 % of the abundance of $ZnS_{(s)}$ or $ZnO_{(s)}$, even under low sulfur conditions. Therefore, this mechanism cannot explain the transition between ZnS and Zn^0 vapour deposition in the Shorty Crater lunar glass bead deposits. We do however note that there is an offset between the temperatures of sublimate deposition predicted in thermochemical models and those observed in natural systems (section 5.2.3).

Our current model does not account for changes in gas cloud chemistry after setting the oxygen fugacity at 1350 °C. It is therefore possible that Zn^0 deposition on 74220 glass beads reflects sulfur depletion caused by Na-K-sulfide condensation (Liu and Ma, 2022). In this scenario, the absence of Na-K-sulfide deposition on 74001,431 glass beads results in insufficient sulfur depletion, preventing Zn^0 deposition.

It is possible that the interiors of the lathe structures on 74001,431 samples contain Zn^0 , as evidenced by excess Zn relative to Si and O. If so, this Zn^0 may be exhibiting a different morphology to Zn^0 on 74220 glass beads. Such morphological differences can result from deposition under different P-T conditions (Renggli and Klemme, 2020; Zelenski and Bortnikova, 2005), or reaction with air (Ma and Liu, 2019a; Liu and Ma, 2022).

We suggest that determining the mineralogy of the volatile-rich, nano-crystalline layer beneath the Zn-chlorohydroxosulfate minerals on 74220 beads could provide insights into P-T-X variations experienced by the orange glass beads as they traversed the volcanic gas plume (Renggli and Klemme, 2020; Zelenski and Bortnikova, 2005).

4.4.2. Vapour deposits at other sites

The volcanic glass beads returned during the Apollo missions can be separated into distinct groups based on composition and crystallinity. Minimally crystallised glass beads display a systematic variation in colour from red to orange, yellow, and green, correlating with decreasing TiO_2 contents (Delano, 1986). Black glass beads are characterised by a higher degree of crystallisation (Weitz et al., 1999).

Compositional variations among the glass bead groups reflect different magmatic sources, partial melting regimes, crystal fractionation processes, and varying extents of crustal contamination (McIntosh et al., 2024; Shearer and Papike, 1993). The surfaces of these bead groups host different condensate phases, potentially reflecting vapour deposition under different volcanic gas plume conditions, or from chemically distinct gas clouds that result from lunar mantle heterogeneity.

To date, sphalerite has not been explicitly identified on lunar glass beads outside the scope of this study. However, ZnS nanocrystals have been reported on yellow, green, and black glasses (Ma and Liu (2023, 2024), Ross et al. (2011)). Ross et al. (2011) described a whisker-like structure predominantly composed of amorphous Zn, capped with Si, on green glass beads from sample 15401. This structure likely corresponds to the ‘lathe’ morphology characterised in this study, which also overlays (Zn, S) micromounds. Additionally, Ross et al. (2011) documented a chemically complex structure that – under secondary electron imaging – matches the ‘plaque’ morphology observed in this work. Collectively, these recurring features suggest a limit to the chemical heterogeneity sampled by lunar pyroclastic volcanism.

Unlike the beads in this study, black glass beads from sample 73001,226 host $NaCl$ above a ZnS layer. This $NaCl$ layer is suggested to have formed during post-depositional fumarolic activity (Liu and Ma, 2024a). Our thermodynamic modelling results suggest that $NaCl$ is likely present in comparable proportions to ZnS when total Na and Zn

abundances within the gas cloud are equal, and melt inclusion analysis suggests that the gas cloud may have contained greater Na than Zn (Hauri et al., 2015; Ni et al., 2019). Our study did not gain sufficient chemical information to identify the beam-sensitive micromounds. However, using observations that $NaCl$ is more susceptible to electron beam damage than ZnS (Liu and Ma, 2024a), we suggest that further compositional analysis may reveal the presence of $NaCl$, providing an avenue for future work. If such work does not detect $NaCl$, this may suggest that sublimate deposition on 74001 black glass beads occurred in a low P-T environment (Fig. 16).

FeS nanocrystals have only been found on yellow glass beads from Apollo sample 15426 (Ma and Liu, 2024). While the limited scope of our study precludes a definitive assessment of FeS nanocrystal presence, their potential absence on 74001,431 glass beads could indicate a lower Zn/Fe ratio in the gas clouds associated with yellow glass bead-forming eruptions compared to orange and green glass beads-forming eruptions.

4.5. Violation of assumptions

4.5.1. Timing of sublimate deposition

Our approach of using sublimates to constrain gas cloud conditions relies on the assumption of a single eruptive event in which sublimate deposition occurs during the flight of glass beads through a single plume. The timescale over which pyroclastic glass beads follow a ballistic trajectory through the gas cloud has been suggested to span seconds to minutes (Florez et al., 2021; Saal et al., 2008), and this timescale aligns with the growth rates of vapour-deposited sphalerite (Benyahia et al., 2015; Ghasemi et al., 2022).

However, sublimate coatings can be produced in three alternative scenarios, which have the potential to undermine our proposition that sublimate mineralogy and layering can be used to determine spatial distributions in P-T-X-f O_2 conditions throughout lunar volcanic gas clouds.

In the first scenario, the sublimates form after the beads have been deposited through fumarolic degassing processes, as described in Liu and Ma (2024a). If this were the case, then all samples would undergo identical post-eruptive mineral deposition, which contradicts the observed diversity of sublimate distributions on different beads. Furthermore, this diversity cannot result from bead mixing processes within the core, as only small-scale reworking is observed in the section of the drive tube from which our samples are derived, despite the impact and potential overturn associated with the excavation of Shorty Crater (Clanton et al., 1978; Meyer, 2010; Weitz III et al., 1996). The limited presence of a second generation of micromounds on surfaces abraded by collisions within the gas cloud (Clanton et al., 1978) also indicates that the majority of vapour deposition must have occurred prior to the collisions and was therefore largely confined to the period before the deposition of beads onto the lunar surface.

In the second scenario, the analysed beads originate from different eruptive phases, or even separate eruptions. In this case, the different sublimate distributions would reflect the different P-T-X-f O_2 conditions associated with each individual eruption, rather than precipitation along different pathways through a single gas cloud. However, we have already discounted the possibility of extensive mixing within the glass bead deposits, which is the only plausible mechanism to bring beads from different eruptions or eruptive phases into proximity with one another. Additionally, the Apollo 17 core deposit was likely produced during one continuous eruption, as the beads exhibit extremely similar chemical compositions throughout the core (Blanchard and Budahn, 1977; Heiken and McKay, 1977).

Finally, the beads may be the result of an impact event, rather than a volcanic eruption. However, this scenario is deemed improbable (Delano, 1986). The sub-millimetre sizes of the glass beads are consistent with theoretical predictions of the consequences of magmatic gas release in vacuum conditions (Wilson and Head, 1981), and the presence of olivine-hosted melt inclusions with the same composition as the host

glasses but significantly higher volatile content supports a magmatic origin of the orange glasses (Hauri et al., 2015).

4.5.2. Alternative Iron enrichment mechanisms

Metal precipitation and space weathering could potentially enrich Fe on the bead surfaces, and thereby undermine the use of Fe vapour-deposition to constrain gas cloud conditions. We consider these scenarios unlikely.

Although sufficient Fe precipitation could deplete bulk Fe in the vapour and force the Fe/Zn ratio in the sublimes to progressively decrease, mass balance calculations indicate that the total mass of the sublimate phase is insufficient for such depletion to occur (Su et al., 2023). Space weathering – resulting from micrometeorite impacts or solar wind irradiation – can generate nanophase iron (npFe^0) particles on glass surfaces through vapour deposition of iron and by inducing a phase change from silicate to metal (Pieters et al., 2000; Sasaki et al., 2001). However, we discount the possibility of Fe-enrichment through space weathering in our samples for several reasons. First, the morphology of the nanophase iron imaged in this study is not consistent with that observed in space-weathered samples (Taylor et al., 2001), and we do not observe nanophase iron clusters within the silicate glass, as would be expected from solar wind damage (Keller and Berger, 2014). Additionally, solar wind irradiation would likely amorphise sphalerite (Bibring et al., 1972), yet we observe a crystalline structure. Although no experimental studies have been conducted on the behaviour of sphalerite under space weathering, simulated solar wind irradiation has been shown to deplete sulfur and enrich iron in Fe-sulfides (Chaves and Thompson, 2022). If sphalerite behaves in a similar manner to Fe-sulfides, iron would be concentrated at the top of the sublimate micromound, rather than at the base. Future studies on the effects of space weathering on sphalerite may therefore be warranted. Finally, space weathering is associated with positive $\delta^{34}\text{S}$ signatures, but the glass bead surface sublimes exhibit negative $\delta^{34}\text{S}$ values (Ding et al., 1983; Saal and Hauri, 2021).

5. Conclusions

Using a variety of nano- and atomic-scale analytical techniques, we characterised the sublimate minerals deposited on the surfaces of pristine Apollo 17 black glass beads.

This analysis revealed a diverse range of morphological forms on the glass bead surfaces, which we identified as micromounds, lathes, plaques, and blebs. We propose that the stratigraphy of these forms – with lathes and blebs overlying micromounds – as well as their different compositions, can be used to investigate pressure and temperature evolution along lunar glass bead trajectories through lunar volcanic gas clouds.

Micromounds, comprised of nano-polycrystalline sphalerite ((Zn, Fe) S), are the most abundant phase on the surface of the beads. Their presence is predicted through equilibrium thermodynamic modelling using the bulk elemental compositions of Renggli et al. (2023) and Varnam et al. (2024), and our findings therefore support current estimates of lunar gas cloud chemistry in which H is more abundant than halogens. The bases of the micromounds are frequently more iron-rich than their upper surfaces, a compositional gradient consistent with deposition along a trajectory from the interior to the exterior of an expanding and cooling gas cloud. Potential $\delta^{34}\text{S}$ depletion during deposition may indicate an increasing degree of kinetic fractionation, also consistent with an expanding gas cloud. Incorporating kinetic effects on condensate deposition will enhance our understanding of the conditions associated with lunar volcanic eruptions.

By comparing zinc deposition as sphalerite in sample 74001,431 to zinc deposition as native Zn⁰ on orange glass beads from sample 74220 (Liu and Ma, 2022; Ma and Liu, 2019b), we propose that glass bead deposits on the rim of Shorty Crater can be used to reconstruct variations

in gas cloud P-T-X conditions during lunar pyroclastic volcanic eruptions.

The observed diversity of sublimate minerals across different studies, even within individual compositional groups of glass beads, highlights the importance of analysing beads throughout the vertical stratigraphy of pyroclastic deposits in future investigations. This approach would enable us to build a more comprehensive understanding of gas-cloud evolution during individual lunar volcanic eruptions. Additionally, such analyses could clarify whether mineralogical variations are driven by gas cloud dynamics, or if they reflect chemical heterogeneity within the lunar mantle.

CRediT authorship contribution statement

T.A. Williams: Writing – review & editing, Writing – original draft, Visualization, Software, Resources, Methodology, Investigation, Formal analysis, Data curation, Conceptualization. **S.W. Parmar:** Writing – review & editing, Supervision, Resources, Project administration, Methodology, Investigation, Funding acquisition, Conceptualization. **A. E. Saal:** Writing – review & editing, Supervision, Resources, Methodology, Investigation, Conceptualization. **A.J. Akey:** Writing – review & editing, Resources, Methodology, Investigation. **J.A. Gardener:** Writing – review & editing, Resources, Methodology, Investigation. **R.C. Ogliore:** Writing – review & editing, Methodology, Investigation.

Declaration of competing interest

The authors declare that they have no known competing financial interests or personal relationships that could have appeared to influence the work reported in this paper.

Acknowledgements

This work was supported by the LunaSCOPE NASA SSERVI node (Grant 80NSSC23M0161). We are very grateful to Olga Prilipko Huber (Brown) for her work on the scientific illustration in Fig. 1. We also thank Dean Khan (Brown) for his help with the thermodynamic modelling work. Finally, we are deeply indebted to Matthew Varnam (University of Edinburgh) and Xue Su (California Institute of Technology) for their deeply insightful comments and feedback.

Appendix A. Supplementary data

Supplementary data to this article can be found online at <https://doi.org/10.1016/j.icarus.2025.116607>.

Data availability

The data, codes, and supplementary files associated with this paper can be found at: <https://doi.org/10.26300/9qr5-c236>

Data from Lunar Volcanic Gas Cloud Evolution: Constraints from Glass Bead Surface Sublimes (Original data) (Brown Digital Repository)

References

- Ali, M.L., Fradet, Q., Riedel, U., 2022. Kinetic mechanism development for the direct reduction of single hematite pellets in H₂/CO atmospheres. Steel Res. Int. 93. <https://doi.org/10.1002/srin.202200043>.
- Arndt, J., Engelhardt, W.V., 1987. Formation of Apollo 17 Orange and Black Glass Beads. J. Geophys. Res. 92 (B4), E372–E376. <https://doi.org/10.1029/JB092iB04p0E372>.
- Arndt, J., Engelhardt, W.V., Gonzalez-Cabeza, I., Meier, B., 1984. Formation of Apollo 15 green glass beads. J. Geophys. Res. Solid Earth 89, C225–C232. <https://doi.org/10.1029/jb089is01p0225>.
- Barton, P.B., Toulmin, P., 1966. Phase relations involving sphalerite in the Fe-Zn system. Econ. Geol. 61, 815–849. <https://doi.org/10.2113/gsecongeo.61.5.815>.

- Benyahia, K., Benhaya, A., Aida, M.S., 2015. ZnS thin films deposition by thermal evaporation for photovoltaic applications. *J. Semicond.* 36, 103001. <https://doi.org/10.1088/1674-4926/36/10/103001>.
- Berkowitz, J., Marquart, J.R., 1963. Equilibrium composition of sulfur vapor. *J. Chem. Phys.* 39, 275–283. <https://doi.org/10.1063/1.1734241>.
- Bibring, J.P., Duraud, J.P., Durrieu, L., Jouret, C., Maurette, M., Meunier, R., 1972. Ultrathin amorphous coatings on lunar dust grains. *Science* 175, 753–755. <https://doi.org/10.1126/science.175.4023.753>.
- Bigeleisen, J., Mayer, M.G., 1947. Calculation of Equilibrium Constants for Isotopic Exchange Reactions. *J. Chem.* 15, 261–267. <https://doi.org/10.1063/1.1746492>.
- Blanchard, M., Balan, E., Schauble, E.A., 2017. Equilibrium Fractionation of Non-traditional Isotopes: a Molecular Modeling Perspective. *Rev. Miner. Geochem.* 82, 27–63.
- Blanchard, D.P., Budahn, J.R., 1977. Chemistry of orange/black soils from core 74001/2. In: *Lunar and Planetary Science Conference*, 9th. Pergamon Press, Inc., pp. 1969–1980.
- Buzatu, A., Bugzari, N., Damian, G., Vasilache, V., Apopei, A.I., 2013. The determination of the Fe content in natural sphalerites by means of Raman spectroscopy. *Vib. Spectrosc.* 68, 220–224. <https://doi.org/10.1016/j.vibspec.2013.08.007>.
- Chaves, L.C., Thompson, M.S., 2022. Space weathering signatures in sulfide and silicate minerals from asteroid Itokawa. *Earth Planets Space* 74, 124. <https://doi.org/10.1186/s40623-022-01683-6>.
- Chou, C.-L., Boynton, W., Sundberg, L., Wasson, J., 1975. Volatiles on the surface of Apollo 15 green glass and trace-element distributions among Apollo 15 soils. *Lunar Science Conference*, 6th, Houston, Tex., March 17–21, 1975, Proceedings. Volume 2 (A78-46668 21-91). Pergamon Press, Inc., New York, pp. 1701–1727.
- Clanton, U., McKay, D., Waits, G., Fuhrman, R., 1978. Sublimate morphology on 74001 and 74002 orange and black glassy droplets. *Lunar and Planetary Science Conference*, 9th, Houston, Tex., March 13–17, 1978, Proceedings. Volume 2. (A79-39176 16-91). Pergamon Press, Inc., New York, pp. 1945–1957.
- Collins, S.M., Midgley, P.A., 2017. Progress and opportunities in EELS and EDS tomography. *Ultramicroscopy* 180, 133–141. <https://doi.org/10.1016/j.ultramic.2017.01.003>.
- Colson, R., 1992. Mineralization on the Moon? Theoretical Considerations of Apollo 16 ‘Rusty Rocks’, Sulfide Replacement in 67016, and Surface-Correlated Volatiles on Lunar Volcanic Glass, pp. 427–436.
- Dauphas, N., Schauble, E.A., 2015. Mass fractionation laws, mass-independent effects, and isotopic anomalies. *Annu. Rev. Earth Planet. Sci.* 44, 1–75. <https://doi.org/10.1146/annurev-earth-060115-012157>.
- Deer, W.A., Howie, R.A., Zussman, J., 2013. An Introduction to the Rock-Forming Minerals. Mineralogical Society of Great Britain and, Ireland. <https://doi.org/10.1180/DHZ>.
- Delano, J.W., 1986. Pristine lunar glasses: criteria, data, and implications. *Proceedings of the sixteenth lunar and planetary science conference, part 2. J. Geophys. Res.* 91, 201–213.
- Delano, J.W., Heiken, G.H., 1990. Proceedings of a Workshop on Lunar Volcanic Glasses—Scientific and Resource Potential.
- Deng, J., Lai, H., Chen, M., Glen, M., Wen, S., Zhao, B., Liu, Z., Yang, H., Liu, M., Huang, L., Guan, S., Wang, P., 2019. Effect of iron concentration on the crystallization and electronic structure of sphalerite/marmatite: a DFT study. *Miner. Eng.* 136, 168–174. <https://doi.org/10.1016/j.mineeng.2019.02.012>.
- Dhara, S., Marceau, R.K.W., Wood, K., Dorin, T., Timokhina, I.B., Hodgson, P.D., 2018. Precipitation and clustering in a Ti-Mn steel investigated using atom probe tomography and small-angle neutron scattering. *Mater. Sci. Eng. A* 718, 74–86. <https://doi.org/10.1016/j.msea.2018.01.070>.
- Ding, T.P., Thode, H.G., Rees, C.E., 1983. Sulphur content and sulphur isotope composition of orange and black glasses in Apollo 17 drive tube 74002/1. *Geochim. Cosmochim. Acta* 47, 491–496. [https://doi.org/10.1016/0016-7037\(83\)90271-5](https://doi.org/10.1016/0016-7037(83)90271-5).
- Dottin, J.W., Kim, S.T., Wing, B., Farquhar, J., Shearer, C., 2023. Anomalous 33S in the lunar mantle. *J. Geophys. Res. Planets* 128. <https://doi.org/10.1029/2022je007597>.
- Downs, R.T., Hall-Wallace, M., 2003. The American mineralogist crystal structure database. *Am. Mineral.* 247–250.
- Edmonds, M., Wallace, P.J., 2017. Volatiles and exsolved vapor in volcanic systems. *Elements* 13, 29–34. <https://doi.org/10.2113/gselements.13.1.29>.
- Egerton, R.F., Li, P., Malac, M., 2004. Radiation damage in the TEM and SEM. *Microsc. Microanal.* 399–409. <https://doi.org/10.1016/j.micron.2004.02.003>.
- Elliot, J.A.W., 2021. Surface thermodynamics at the nanoscale. *J. Chem. Phys.* 154, 190901. <https://doi.org/10.1063/5.0049031>.
- Fegley, B., 1991. Thermodynamic models of the chemistry of lunar volcanic gases. *Geophys. Res. Lett.* 18, 2073–2076. <https://doi.org/10.1029/91gl02624>.
- Florez, D., Huber, C., Milliken, R.E., Berkson, J., 2021. Modeling lunar pyroclasts to probe the volatile content of the lunar interior. *J. Geophys. Res. Planets* 126. <https://doi.org/10.1029/2020je006645>.
- Ghasemi, H., Mozaffari, M.H., Moradian, R., 2022. Effects of deposition time on structural and optical properties of ZnS and ZnS/Au thin films grown by thermal evaporation. *Phys. B Condens. Matter* 627, 413616. <https://doi.org/10.1016/j.physb.2021.413616>.
- Goldberg, R.H., Burnett, D.S., Tombrello, T.A., 1975. Fluorine surface films on lunar samples - Evidence for both lunar and terrestrial origins. In: *Lunar Science Conference*, 6th, Houston, Tex.
- Gopon, P., Douglas, J.O., Auger, M.A., Hansen, L., Wade, J., Cline, J.S., Robb, L.J., Moody, M.P., 2019. A nanoscale investigation of Carlin-type gold deposits: an atomic-scale elemental and isotopic perspective. *Econ. Geol.* 114, 1123–1133. <https://doi.org/10.5382/econgeo.4676>.
- Green, D.H., Ringwood, A.E., Hibberson, W.O., Ware, N.G., 1975. Experimental petrology of Apollo 17 mare basalts. In: *Lunar and Planetary Science Conference Proceedings*, 1, pp. 871–893.
- Hashimoto, A., 1990. Evaporation kinetics of forsterite and implications for the early solar nebula. *Nature* 347, 53–55. <https://doi.org/10.1038/347053a0>.
- Hatzoglou, C., Rouland, S., Radiguet, B., Etienne, A., Costa, G.D., Sauvage, X., Pareige, P., Vurpillot, F., 2020. Preferential evaporation in atom probe tomography: an analytical approach. *Microsc. Microanal.* 26, 689–698. <https://doi.org/10.1017/s1431927620001749>.
- Hauri, E.H., Weinreich, T., Saal, A.E., Rutherford, M.C., Orman, J.A.V., 2011. High pre-eruptive water contents preserved in lunar melt inclusions. *Science* 333, 213–215. <https://doi.org/10.1126/science.1204626>.
- Hauri, E.H., Saal, A.E., Rutherford, M.J., Orman, J.A.V., 2015. Water in the moon’s interior: truth and consequences. *Earth Planet. Sci. Lett.* 409, 252–264. <https://doi.org/10.1016/j.epsl.2014.10.053>.
- Head, J.W., Wilson, L., 2017. Generation, ascent and eruption of magma on the moon: new insights into source depths, magma supply, intrusions and effusive/explosive eruptions (part 2: predicted emplacement processes and observations). *Icarus* 283, 176–223. <https://doi.org/10.1016/j.icarus.2016.05.031>.
- Head, J.W., Wilson, L., Deutsch, A.N., Rutherford, M.J., Saal, A.E., 2020. Volcanically induced transient atmospheres on the moon: assessment of duration, significance, and contributions to polar volatile traps. *Geophys. Res. Lett.* 47. <https://doi.org/10.1029/2020gl089509>.
- Heiken, G.H., McKay, D.S., 1977. A model for eruption behavior of a volcanic vent in eastern Mare Serenitatis. In: *Lunar Science Conference*, 8th.
- Heiken, G.H., McKay, D.S., Brown, R.W., 1974. Lunar deposits of possible pyroclastic origin. *Geochim. Cosmochim. Acta* 38, 1703–1718. [https://doi.org/10.1016/0016-7037\(74\)90187-2](https://doi.org/10.1016/0016-7037(74)90187-2).
- Henley, R.W., Berger, B.R., 2013. Nature’s refineries — metals and metalloids in arc volcanoes. *Earth Sci. Rev.* 125, 146–170. <https://doi.org/10.1016/j.earscirev.2013.07.007>.
- Hui, H., Hess, K.-U., Zhang, Y., Nichols, A.R.L., Peslier, A.H., Lange, R.A., Dingwell, D.B., Neal, C.R., 2018. Cooling rates of lunar orange glass beads. *Earth Planet. Sci. Lett.* 503, 88–94. <https://doi.org/10.1016/j.epsl.2018.09.019>.
- Iacovino, K., 2022. Calculate fO2 Buffer (1.5). Zenodo. <https://doi.org/10.5281/zenodo.7387196>.
- Keller, L.P., Berger, E.L., 2014. A transmission electron microscope study of Itokawa regolith grains. *Earth Planets Space* 66, 71. <https://doi.org/10.1186/s40800-014-0066-7>.
- Kilburn, M.R., Clode, P.L., 2013. Elemental and Isotopic Imaging of Biological Samples Using NanoSIMS, in: *Methods in Molecular Biology, Methods in Molecular Biology*. <https://doi.org/10.1007/978-1-62703-776-1>.
- King, P.L., Wheeler, V.M., Renggli, C.J., Palm, A.B., Wilson, S.A., Harrison, A.L., Morgan, B., Nekvasil, H., Troitzsch, U., Mernagh, T., Yue, L., Bayon, A., DiFrancesco, N.J., Baile, R., Kreider, P., Lipiński, W., 2018. Gas-solid reactions: theory, experiments and case studies relevant to earth and planetary processes. *Rev. Mineral. Geochem.* 84, 1–56. <https://doi.org/10.2138/rmg.2018.84.1>.
- Kita, N.T., Ushikubo, T., Fu, B., Valley, J.W., 2009. High precision SIMS oxygen isotope analysis and the effect of sample topography. *Chem. Geol.* 264, 43–57. <https://doi.org/10.1016/j.chemgeo.2009.02.012>.
- Kring, D.A., Kramer, G.Y., Bussey, D.B.J., Hurley, D.M., Stickle, A.M., van der Bogert, C. H., 2021. Prominent volcanic source of volatiles in the south polar region of the moon. *Adv. Space Res.* 68, 4691–4701. <https://doi.org/10.1016/j.asr.2021.09.008>.
- Lee, K.M., Cai, Z., Griggs, J.A., Guiatas, L., Lee, D.J., Okabe, T., 2004. SEM/EDS evaluation of porcelain adherence to gold-coated cast titanium. *J. Biomed. Mater. Res. Part B: Appl. Biomater.* 68B, 165–173. <https://doi.org/10.1002/jbm.b.20017>.
- Li, Y., Liu, J., 2006. Calculation of sulfur isotope fractionation in sulfides. *Geochim. Cosmochim. Acta* 70, 1789–1795. <https://doi.org/10.1016/j.gca.2005.12.015>.
- Liu, Y., Ma, C., 2022. Direct evidence of volcanic outgassing of Na and K on the moon from Apollo orange beads. *Icarus* 382. <https://doi.org/10.1016/j.icarus.2022.115044>.
- Liu, Y., Ma, C., 2024a. Vapor condensates on the most pristine black beads from a clod in Apollo drive tube 73001: discovery of lunar NaCl nanocrystals. *J. Geophys. Res. Planets* 129. <https://doi.org/10.1029/2024je008444>.
- Liu, Y., Ma, C., 2024b. Discovery of Lunar Halite Nanocrystals on the Surface of a Black Bead from Apollo 73001, 226, in: *55th Lunar and Planetary Science Conference*.
- Liu, Y., Ma, C., Housley, R.M., 2020. Contrasting Volcanic Gases Between Pyroclastic Eruptions on the Moon. *51st Lunar and Planetary Science Conference*.
- Lusk, J., Calder, B.O.E., 2004. The composition of sphalerite and associated sulfides in reactions of the Cu-Fe-Zn-S, Fe-Zn-S and Cu-Fe-S systems at 1 bar and temperatures between 250 and 535 °C. *Chem. Geol.* 203, 319–345. <https://doi.org/10.1016/j.chemgeo.2003.10.011>.
- Ma, C., Liu, Y., 2019a. Discovery of a zinc-rich mineral on the surface of lunar orange pyroclastic beads. *Am. Mineral.* 104, 447–452. <https://doi.org/10.2138/am-2019-6896>.
- Ma, C., Liu, Y., 2019b. Nanomineralogy of Lunar Orange Beads: Discovery of a Zinc-Rich Mineral (Probably Gordaite), Derived from Volcanic Vapor Condensates on the Moon. *50th Lunar and Planetary Science Conference, Abstract #1463*.
- Ma, C., Liu, Y., 2023. Nanomineralogy of Lunar Beads: Discovery of Zinc Sulfide (ZnS) Nanocrystals on a Yellow Bead Fragment, Condensed From Volcanic Vapors on the Moon. In: *54th Lunar and Planetary Science Conference*.
- Ma, C., Liu, Y., 2024. Nanomineralogy of lunar beads: Discovery of FeS nanocrystals on yellow beads, condensed from volcanic vapors on the Moon. In: *55th Lunar and Planetary Science Conference, Abstract #1347*.

- McCanta, M.C., Dyar, M.D., Lanzirotti, A., Newville, M., Breitenfeld, L.B., 2019. In-situ mapping of ferric iron variations in lunar glasses using X-ray absorption spectroscopy. *Am. Minerol.* 104, 453–458. <https://doi.org/10.2138/am-2019-6863>.
- McIntosh, E.C., Day, J.M.D., McCubbin, F.M., Kaaden, K.E.V., Hattingh, R., Porrrachia, M., 2024. Revisiting the petrogenesis of pyroclastic glass bead deposits at the Apollo 15 and 17 sites. *J. Pet.* 65, ega026. <https://doi.org/10.1093/petrology/egae026>.
- McKay, D.S., Wentworth, S.J., 1992. Morphology and composition of condensates on Apollo 17 orange and black glass. In: *Lunar Science Inst., Workshop on Geology of the Apollo 17 Landing Site*.
- McKay, D.S., Clanton, U.S., Ladle, G., 1973. Scanning electron microscope study of Apollo 15 green glass. In: *Proceedings of the Lunar Science Conference*, 4, pp. 225–238.
- Merli, P.G., Morandi, V., Corticelli, F., 2003. Backscattered electron imaging and scanning transmission electron microscopy imaging of multi-layers. *Ultramicroscopy* 94, 89–98. [https://doi.org/10.1016/s0304-3991\(02\)00217-6](https://doi.org/10.1016/s0304-3991(02)00217-6).
- Meyer, C., 2010. Lunar Sample Compendium - 74220 (online). Retrieved from: <https://www.lpi.usra.edu/lunar/samples/atlas/compendium/74220.pdf>.
- Meyer Jr., C., McKay, D.S., Anderson, D.H., Butler Jr., P., 1975. The source of sublimes on the Apollo 15 green and Apollo 17 orange glass samples. *Lunar Sci. Conf.* 6th, 1674–1699.
- Moussallam, Y., Edmonds, M., Scaillet, B., Peters, N., Gennaro, E., Sides, I., Oppenheimer, C., 2016. The impact of degassing on the oxidation state of basaltic magmas: a case study of Kilauea volcano. *Earth Planet. Sci. Lett.* 450, 317–325. <https://doi.org/10.1016/j.epsl.2016.06.031>.
- Nagle, J.S., 1978. A comparison of a lunar and a terrestrial volcanic section. In: *Lunar and Planetary Science Conference Proceedings*, pp. 1509–1526.
- Ni, P., Zhang, Y., Chen, S., Gagnon, J., 2019. A melt inclusion study on volatile abundances in the lunar mantle. *Geochim. Cosmochim. Acta* 249, 17–41. <https://doi.org/10.1016/j.gca.2018.12.034>.
- Pasek, J., Tahk, A., 2021. Weighting and Weighted Statistics. <https://cran.r-project.org/package=weights>.
- Pieters, C.M., Taylor, L.A., Noble, S.K., Keller, L.P., Hapke, B., Morris, R.V., Allen, C.C., McKay, D.S., Wentworth, S., 2000. Space weathering on airless bodies: resolving a mystery with lunar samples. *Meteorit. Planet. Sci.* 35, 1101–1107. <https://doi.org/10.1111/j.1945-5100.2000.tb01496.x>.
- Pokrovski, G.S., Borisova, A.Y., Bychkov, A.Y., 2013. Speciation and transport of metals and metalloids in geological vapors. *Rev. Mineral. Geochem.* 76, 165–218. <https://doi.org/10.1013/rmg.2013.76.6>.
- Prosa, T.J., Strennen, S., Olson, D., Lawrence, D., Larson, D.J., 2019. A study of parameters affecting atom probe tomography specimen survivability. *Microsc. Microanal.* 25, 425–437. <https://doi.org/10.1017/s1431927618015258>.
- R Core Team, 2024. R: A Language and Environment for Statistical Computing. R Foundation for Statistical Computing, Vienna, Austria. <https://www.R-project.org/>.
- Reddy, S.M., Saxe, D.W., Rickard, W.D.A., Fougerouse, D., Montalvo, S.D., Verberne, R., van Riessen, A., 2020. Atom probe tomography: development and application to the geosciences. *Geostand. Geoanal. Res.* 44, 5–50. <https://doi.org/10.1111/ggr.12313>.
- Renggli, C.J., Klemme, S., 2020. Experimental constraints on metal transport in fumarolic gases. *J. Volcanol. Geotherm. Res.* 400. <https://doi.org/10.1016/j.jvolcanol.2020.106929>.
- Renggli, C.J., King, P.L., Henley, R.W., Norman, M.D., 2017. Volcanic gas composition, metal dispersion and deposition during explosive volcanic eruptions on the moon. *Geochim. Cosmochim. Acta* 206, 296–311. <https://doi.org/10.1016/j.gca.2017.03.012>.
- Richet, P., Bottinga, Y., Jayov, M., 1977. A review of hydrogen, carbon, nitrogen, oxygen, sulphur, and chlorine stable isotope fractionation among gaseous molecules. *Annu. Rev. Earth Planet. Sci.* 5, 65–110. [https://doi.org/10.1146/annurev.ea.05.050177.000433](https://doi.org/10.1146/annurev. ea.05.050177.000433).
- Ross, K., Thomas-Keptra, K.L., Rahman, Z., Wentworth, S.J., McKay, D.S., 2011. FE-SEM, FIB and TEM Study of Surface Deposits on Apollo 15 Green Glass Volcanic Spherules. *42nd Lunar and Planetary Science Conference*.
- Rousseau, L., Normand, A., Morgado, F.F., Søreide, H.-S.M.S., Stephenson, L.T., Hatzoglou, C., Costa, G.D., Tehrani, K., Freysoldt, C., Gault, B., Vurpillot, F., 2023. Introducing field evaporation energy loss spectroscopy. *Commun. Phys.* 6, 100. <https://doi.org/10.1038/s42005-023-01203-2>.
- Rutherford, M.K., Head, J.W., Saal, A.E., Hauri, E., Wilson, L., 2017. Model for the origin, ascent, and eruption of lunar picritic magmas. *Am. Mineral.* <https://doi.org/10.2138/am-2017-5994cbynncnd>.
- Saal, A.E., Hauri, E.H., 2021. Large sulfur isotope fractionation in lunar volcanic glasses reveals the magmatic differentiation and degassing of the Moon. *Sci. Adv.* 7. <https://doi.org/10.1126/sciadv.abe4641>.
- Saal, A.E., Hauri, E.H., Cascio, M.L., Orman, J.A.V., Rutherford, M.C., Cooper, R.F., 2008. Volatile content of lunar volcanic glasses and the presence of water in the moon's interior. *Nature* 454, 192–195. <https://doi.org/10.1038/nature07047>.
- Sabri, T., Gavilan, L., Jäger, C., Lemaire, J.L., Vidali, G., Mutschke, H., Henning, T., 2014. Interstellar silicate analogs for grain-surface reaction experiments: gas-phase condensation and characterization of the silicate dust grains. *Astrophys. J.* 780, 180. <https://doi.org/10.1088/0004-637x/780/2/180>.
- Sasaki, S., Nakamura, K., Hamabe, Y., Kurahashi, E., Hiroi, T., 2001. Production of iron nanoparticles by laser irradiation in a simulation of lunar-like space weathering. *Nature* 410, 555–557. <https://doi.org/10.1038/35069013>.
- Sharp, Z.D., Shearer, C.K., McKeegan, K.D., Barnes, J.D., Wang, Y.Q., 2010. The chlorine isotope composition of the moon and implications for an anhydrous mantle. *Science* 329, 1050–1053. <https://doi.org/10.1126/science.1192606>.
- Sharp, Z.D., McCubbin, F.M., Shearer, C.K., 2013. A hydrogen-based oxidation mechanism relevant to planetary formation. *Earth Planet. Sci. Lett.* 380, 88–97. <https://doi.org/10.1016/j.epsl.2013.08.015>.
- Shearer, C.K., Papike, J.J., 1993. Basaltic magmatism on the moon: a perspective from volcanic picritic glass beads. *Geochim. Cosmochim. Acta* 57, 4785–4812. [https://doi.org/10.1016/0016-7037\(93\)90200-g](https://doi.org/10.1016/0016-7037(93)90200-g).
- Snyder, G.A., Taylor, L.A., Neal, C.R., 1992. A chemical model for generating the sources of mare basalts: Combined equilibrium and fractional crystallization of the lunar magmasphere, 56, pp. 3809–3823. [https://doi.org/10.1016/0016-7037\(92\)90172-f](https://doi.org/10.1016/0016-7037(92)90172-f).
- Steenstra, E.S., Berndt, J., Klemme, S., Fei, Y., van Westrenen, W., 2020. A possible high-temperature origin of the moon and its geochemical consequences. *Earth Planet. Sci. Lett.* 538, 116222. <https://doi.org/10.1016/j.epsl.2020.116222>.
- Su, X., Zhang, Y., Liu, Y., 2025. Sulfur Outgassing and in-Gassing in Lunar Orange Glass Beads and Implications for 3S3S "Anomaly" in the Moon. *Geochim. Cosmochim. Acta*. <https://doi.org/10.1016/j.gca.2025.03.026>.
- Su, X., Zhang, Y., Liu, Y., Holder, R.M., 2023. Outgassing and in-gassing of Na, K and Cu in lunar 74220 orange glass beads. *Earth Planet. Sci. Lett.* 602, 117924. <https://doi.org/10.1016/j.epsl.2022.117924>.
- Su, X., Zhang, Y., 2024. Volatiles in melt inclusions from lunar mare basalts: Bridging the gap in the H2O/Ce ratio between melt inclusions in lunar pyroclastic sample 74220 and other mare samples. *Geochim. Cosmochim. Acta* 373, 232–244. <https://doi.org/10.1016/j.gca.2024.04.002>.
- Subramani, T., Lilova, K., Householder, M., Yang, S., Lyons, J., Navrotsky, A., 2023. Surface energetics of wurtzite and sphalerite polymorphs of zinc sulfide and implications for their formation in nature. *Geochim. Cosmochim. Acta* 340, 99–107. <https://doi.org/10.1016/j.gca.2022.11.003>.
- Taylor, L.A., Pieters, C.M., Keller, L.P., Morris, R.V., McKay, D.S., 2001. Lunar Mare Soils: Space weathering and the major effects of surface-correlated nanophasic Fe. *J. Geophys. Res. Planets* 106, 27985–27999. <https://doi.org/10.1029/2000je001402>.
- Thompson, K., Lawrence, D., Larson, D.J., Olson, J.D., Kelly, T.F., Gorman, B., 2007. In situ site-specific specimen preparation for atom probe tomography. *Ultramicroscopy* 107, 131–139. <https://doi.org/10.1016/j.ultramic.2006.06.008>.
- Thode, H.G., Rees, C.E., 1976. Sulphur isotopes in grain size fractions of lunar soils. *Lunar Science Conference*, 7th, pp. 459–468.
- Ustunisik, G., Nekvasil, H., Lindsley, D.H., 2011. Experimental Determination of Degassing Paths of Volatiles from Lunar Magmas: New Insights from Time Studies, in: *41st Lunar and Planetary Science Conference*.
- Ustunisik, G., Nekvasil, H., Lindsley, D.H., McCubbin, F.M., 2015. Degassing Pathways of Cl-, F-, H-, and S-Bearing Magmas near the Lunar Surface: Implications for the Composition and Cl Isotopic Values of Lunar Apatite. Walter de Gruyter GmbH, pp. 1717–1727. <https://doi.org/10.2138/am-2015-4883>.
- Varnam, M., Hamilton, C.W., Aleinov, I., Barnes, J.J., 2024. Composition and speciation of volcanic volatiles on the moon. *Icarus* 413, 116009. <https://doi.org/10.1016/j.icarus.2024.116009>.
- Wadhwa, M., 2008. Redox conditions on small bodies, the moon and mars. *Rev. Mineral. Geochem.* 68, 493–510. <https://doi.org/10.2138/rmg.2008.68.17>.
- Wahreberger, C., Seward, T.M., Dietrich, V., 2002. Volatile trace-element transport in high-temperature gases from Kudriavy volcano (Iturup, Kurile Islands, Russia). In: Hellmann, R., Wood, S.A. (Eds.), *Water-Rock Interactions, Ore Deposits, and Environmental Geochemistry: A Tribute to David A. Crerar*. The Geochemical Society, Special Publication No. 7.
- Wasson, J., 1976. Volatile Compounds Released During Lunar Lava Fountaining, in: *Lunar Science Conference*, 7th, pp. 1583–1595.
- Weitz III, C.M., J.W.H., McKay, D.S., 1996. Eruption and emplacement of lunar pyroclastic glasses as inferred from the 74001/2 section. *Lunar Planet. Sci.* 27, 1411–1412.
- Weitz, C.M., Rutherford, M.J., Head, J.W., 1997. Oxidation states and ascent history of the Apollo 17 volcanic beads as inferred from metal-glass equilibria. *Geochim. Cosmochim. Acta* 61, 2765–2775. [https://doi.org/10.1016/s0016-7037\(97\)00119-1](https://doi.org/10.1016/s0016-7037(97)00119-1).
- Weitz, C.M., Rutherford, M.J., Head III, J.W., McKay, D.S., 1999. Ascent and eruption of a lunar high-titanium magma as inferred from the petrology of the 74001/2 drill core. *Meteorit. Planet. Sci.* 34, 527–540. <https://doi.org/10.1111/j.1945-5100.1999.tb01361.x>.
- Wetzel, D.T., Hauri, E.H., Saal, A.E., Rutherford, M.J., 2015. Carbon content and degassing history of the lunar volcanic glasses. *Nat. Geosci.* 8, 755–758. <https://doi.org/10.1038/ngeo2511>.
- Wilson, L., Head, J.W., 1981. Ascent and eruption of basaltic magma on the earth and moon. *J. Geophys. Res. Solid Earth* 86, 2971–3001. <https://doi.org/10.1029/jb086ib04p02971>.
- Wilson, L., Head, J.W., 2018. Controls on lunar basaltic volcanic eruption structure and morphology: gas release patterns in sequential eruption phases. *Geophys. Res. Lett.* 45, 5852–5859. <https://doi.org/10.1029/2018gl078327>.
- Woods, E.V., Singh, M.P., Kim, S.-H., Schwarz, T.M., Douglas, J.O., El-Zoka, A.A., Giulani, F., Gault, B., 2023. A versatile and reproducible cryo-sample preparation methodology for atom probe studies. *Microsc. Microanal.* 29, 1992–2003. <https://doi.org/10.1093/micmic/ozad120>.
- Zeleniski, M., Bortnikova, S., 2005. Sublimate speciation at Mutnovsky volcano, Kamchatka. *Eur. J. Mineral.* 17, 107–118. <https://doi.org/10.1127/0935-1221/2005/0017-107>.